MERCURY DIMER SPECTROSCOPY

AND AN EINSTEIN-PODOLSKY-ROSEN EXPERIMENT

A Dissertation

by

XINMEI QU

Submitted to the Office of Graduate Studies of
Texas A&M University
in partial fulfillment of the requirements for the degree of

DOCTOR OF PHILOSOPHY

August 2008

Major Subject: Physics

MERCURY DIMER SPECTROSCOPY

AND AN EINSTEIN-PODOLSKY-ROSEN EXPERIMENT

A Dissertation

by

XINMEI QU

Submitted to the Office of Graduate Studies of
Texas A&M University
in partial fulfillment of the requirements for the degree of

DOCTOR OF PHILOSOPHY

Approved by:

Chair of Committee,	Edward S. Fry
Committee Members,	Jaan Laane
	George W. Kattawar
	Alexei Sokolov
Head of Department,	Edward S. Fry

August 2008

Major Subject: Physics

ABSTRACT

Mercury Dimer Spectroscopy

and an Einstein-Podolsky-Rosen Experiment. (August 2008)

Xinmei Qu, B.S., Shandong University;

M.S., Shandong University

Chair of Advisory Committee: Dr. Edward S. Fry

The dissociation of a $^{199}Hg_2$ dimer prepares an entangled state of two spatially separated ^{199}Hg atoms, each with nuclear spin 1/2, and with zero total electron and nuclear spin angular momenta. This is identical to the entangled state of the two spin 1/2 particles in Bohm's classic version of the EPR *gedankenexperiment*. An analysis of the rotational structure of the $\upsilon'=57\leftarrow\upsilon''=0$ band of the $D^3\Sigma_u^+(1_u)\leftarrow X^1\Sigma_g^+(0_g^+)$ transition in Hg_2 (natural abundance) is presented. The analysis of the fluorescence excitation spectrum using a dye laser gives the values of the constants $B_{\upsilon'=57}$ and $B_{\upsilon''=0}$ for the excited and ground electronic energy states involved in the transition, respectively. To increase the accuracy of the rotational constants and resolve the fine spectrum of the Hg_2, a continuously tunable single longitudinal mode laser with ultra-narrow line-width is needed. Measurements using a narrow line-width alexandrite laser had been attempted and the values of $B_{\upsilon'=57}$ and $B_{\upsilon''=0}$ were determined. To improve the quality of the laser beam and hence the precision of the rotational constants, modifications have been made to the cavity of the alexandrite laser. This provides a possibility for further investigation.

To My Husband

ACKNOWLEDGMENTS

Thanks to my advisor, Dr. Edward S. Fry, for all the support, enlightening suggestions and great encouragement. I would like to thank all my committee members, Dr. George W. Kattawar, Dr. Alexei Sokolov, Dr. Jaan Laane, Dr. Yi-Qin Gao, Dr. Robert A. Kenefick, Dr. Henry F. Taylor, Dr. Thomas Walther, and Dr. Robert Lucht for expertise, encouragement, helpful discussions and comments.

Special thanks to my colleagues, Dr. Jaroslaw Koperski and Dr. Hongxing Meng, who worked with me on the dimer spectroscopy measurements using a dye laser.

Support from the Machine Shop and Electronics Shop of the Department of Physics is gratefully acknowledged; especially thanks to Chuck Hale and Tom Weimar.

I reserve my final thanks for Zheng Lu, not only my husband who supports me all the time, but also my colleague sparing no effort to help me in the lab.

TABLE OF CONTENTS

Page

CHAPTER Page

LIST OF FIGURES

Page

Page

Page

LIST OF TABLES

CHAPTER I

INTRODUCTION

1.1 Einstein-Podolsky-Rosen Experiment

1.1.1 Background and the Historical Review

In the early years of the successful development of quantum mechanics, many people expressed a great concern about the interpretation of quantum mechanics for single microscopic systems.

In 1935, Albert Einstein together with Boris Podolsky and Nathan Rosen (generally referred to as EPR) wrote a paper in which they expressed their concern that quantum mechanics was an incomplete theory[1] and additional parameters, "hidden variables", should be required in order to restore the completeness of the theory. In 1964, John Bell published the proof that any hidden variable theory satisfying a physically reasonable condition of locality will yield statistical predictions that must satisfy restrictions for certain correlated phenomena;[2] these restrictions can be violated by the statistical prediction of quantum mechanics. These restrictions are referred to as Bell inequalities. In 1969, Clauser *et al.* introduced auxiliary assumptions to make physically realizable experiments possible with existing technology.[3] From then on, several experiments were performed[4-13] but all of these experiments required an auxiliary assumption since they involved photons in or near the visible spectrum where the efficiencies of the detectors were typically <20%. An inequality that can be tested experimentally with no auxiliary assumptions is called a strong Bell, an

---

This dissertation follows the style of Applied Optics.

example was provided by Clauser and Horne in 1974.[4,14] However, the quantum mechanical predictions will only violate the inequality for very high detector efficiencies. Strong Bell inequalities have not yet been tested experimentally.

1.1.2 A Loophole-free Test of the Bell Inequalities

The wavefunction of a diatomic homonuclear molecule (dimer) consisting of two ^{199}Hg atoms, each with nuclear spin 1/2, and with zero total electron and nuclear spin angular momenta is identical to the entangled state of the two spin 1/2 particles in Bohm's classic spin-1/2 particle version of the EPR experiment.[15] In a practical implementation, the $^{199}Hg_2$ dimers are produced in a supersonic beam, and those with total nuclear spin $\boldsymbol{I}$=0 (*i.e.* such that the entangled state of the two ^{199}Hg atoms is a singlet), are selectively excited at a carefully chosen rotational transition and then dissociated by two 266 nm and 355 nm laser

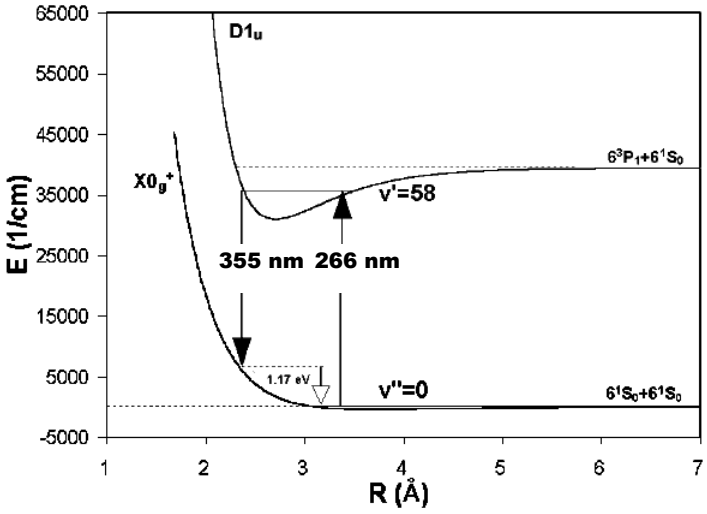

Figure I-1. Energy levels of a mercury dimer and the relevant transitions leading to dissociation.

beams, respectively. See Fig. I-1.

The measurement of nuclear spin correlations between the two spatially separated atoms is then achieved by detection of the atoms using a spin state selective two-photon excitation-ionization scheme.[16] The detection efficiency is sufficient to close the detector efficiency loophole.

An essential part of the experiment is the preparation of the two ^{199}Hg atoms in an entangled state with total nuclear spin $\boldsymbol{I}$=0. This is achievable but requires that the rotational structure of the ^{199}Hg^{199}Hg molecule be carefully investigated and analyzed. This is the main thrust of this work.

1.2 Ti:Sapphire Laser and Deformable Mirror

A Ti: Sapphire laser, injection seeded simultaneously with two laser diodes[17] at 789.2 nm and 761.1 nm, is chosen for the detection laser in the loophole-free EPR experiment. The excitation laser at 253.7 nm can be obtained from the third harmonic of 761.1 nm and the ionizing laser at 197.3 nm from the fourth harmonic of 789.2 nm. The harmonic generation requires a high quality laser beam especially for high order harmonic generation. To improve the output from the Ti:Sapphire laser and increase the harmonic generation efficiency, we made a piezoelectric deformable mirror which will replace one of the cavity mirrors[18]. It's construction consists of a very thin mirror (250 microns) coated at the lasing wavelength and 12 × 12 discrete actuators perpendicular to the surface with a 1 mm center-spacing. The actuators are made of piezoelectric ceramics which convert electrical signals into mechanical displacement. Each actuator is connected to the membrane with a small

steel ball interface in order to obtain desirable deformation characteristics. The other ends of the actuators are bonded to a rigid common base. The actuators are segments cut from the same piece of material in order to obtain as nearly uniform properties as possible. Each actuator is 2.312″ long, 0.015″ thick and 0.030″ wide. Each actuator can be adjusted mechanically and electrically corresponding to coarse and fine adjustments, respectively.

CHAPTER II

TOTAL ENERGY AND THE ROTATIONAL STRUCTURE

2.1 Total Energy

To interpret experimental observations in molecular spectroscopy, the anharmonically vibrating non-rigid rotator is the model used most often for nuclear motion in diatomic molecule. To a first approximation, the electronic and nuclear (vibrational and rotational) motions in the molecule can be treated independently. The Schrödinger equation of a diatomic molecule may be written as[19]

$$\frac{1}{m}\sum_i\left(\frac{\partial^2\psi}{\partial x_i^2}+\frac{\partial^2\psi}{\partial y_i^2}+\frac{\partial^2\psi}{\partial z_i^2}\right)+\sum_k\frac{1}{M_k}\left(\frac{\partial^2\psi}{\partial x_k^2}+\frac{\partial^2\psi}{\partial y_k^2}+\frac{\partial^2\psi}{\partial z_k^2}\right)+\frac{8\pi^2}{h^2}(E-V)\psi=0, \qquad (2.1)$$

where, x_i, y_i, z_i are the coordinates of the electrons (mass m) and x_k, y_k, z_k are those of the nuclei (mass M_k). Substituting the approximate solution

$$\psi=\psi_e(\cdots,x_i,y_i,z_i,\cdots)\psi_{vr}(\cdots,x_k,y_k,z_k,\cdots), \qquad (2.2)$$

where ψ_e is the eigenfunction of the electrons and ψ_{vr} the eigenfunction of the vibrating rotator, into Eq. (2.1), we get

$$\sum_i\left(\frac{\partial^2\psi_e}{\partial x_i^2}+\frac{\partial^2\psi_e}{\partial y_i^2}+\frac{\partial^2\psi_e}{\partial z_i^2}\right)+\frac{8\pi^2 m}{h^2}(E^{el}-V_e)\psi_e=0 \qquad (2.3)$$

and

$$\sum_k\frac{1}{M_k}\left(\frac{\partial^2\psi_{vr}}{\partial x_k^2}+\frac{\partial^2\psi_{vr}}{\partial y_k^2}+\frac{\partial^2\psi_{vr}}{\partial z_k^2}\right)+\frac{8\pi^2}{h^2}(E-E^{el}-V_n)\psi_{vr}=0, \qquad (2.4)$$

Where E^{el} *is* the energy of the electrons; m is the mass of the electrons; M_k is the mass of the nuclei.

The first of these equations is the Schrödinger equation for electrons moving in the field of the fixed nuclei (with potential energy V_e). The second equation is the Schrödinger equation of the nuclei moving under the action of the potential $E^{el} + V_n$ where V_n is the Coulomb potential energy of the nuclei.

The total energy E of the molecule is, to a very good approximation, a sum of three components,[19]

$$E = E_e + E_{vib} + E_{rot}, \tag{2.5}$$

where E_e, E_{vib} and E_{rot} are the electronic, vibrational and rotational energies, respectively. Here E_e is the minimum value of $E^{el} + V_n$.

Traditionally, the energy is expressed in wave number units (cm^{-1}), and Eq. (2.5) can be rewritten using so-called term values,

$$T = T_e + G(v) + F_v(J), \tag{2.6}$$

where T_e, $G(v)$ and $F_v(J)$ are electronic, vibrational and rotational terms, respectively. The vibrational term can be expressed as

$$G(v) = \omega_e(v+\frac{1}{2}) - \omega_e\chi_e(v+\frac{1}{2})^2 + \omega_e y_e(v+\frac{1}{2})^3 + \cdots, \tag{2.7}$$

Where ω_e , $\omega_e\chi_e$ and $\omega_e y_e$ are vibrational frequency (from the harmonic oscillator approximation), single anharmonicity and "second-order" anharmonicity, respectively. The rotational term can be expressed as

$$F_v(J) = B_v J(J+1) - D_v J^2 (J+1)^2 + \cdots, \tag{2.8}$$

where B_v and D_v are rotational constants. For a particular v, the B_v and D_v are defined as follows:

$$B_v = B_e - \alpha_e (v + \frac{1}{2}) + \cdots, \tag{2.9}$$

and

$$D_v = D_e - \beta_e (v + \frac{1}{2}) + \cdots, \tag{2.10}$$

where B_e and D_e are rotational and centrifugal constants, respectively, at the equilibrium position ($R = R_e$); note $B_e << D_e$.

$$B_e = \frac{\mathrm{h}}{8\pi^2 \mathrm{c} \mu R_e^2} \tag{2.11}$$

and for the case of harmonic oscillator,

$$\mathrm{D}_e = \frac{4B_e^3}{\omega_e^2}. \tag{2.12}$$

If one assumes that the molecular potential of an electronic state is represented by a Morse function,[20] the factors α_e can be expressed by the so-called Pekeris relation[21]

$$\alpha_e = \frac{6B_e}{\omega_e}\left(\sqrt{\omega_e x_e B_e} - B_e\right) \tag{2.13}$$

and β_e may be written as[22]

$$\beta_e = D_e\left(\frac{8\omega_e x_e}{\omega_e} - \frac{5\alpha_e}{B_e} - \frac{\alpha_e^2 \omega_e}{24 B_e^3}\right). \tag{2.14}$$

Then the wave numbers of the transitions between two energy levels are given by

$$\upsilon = T' - T'' = (T_e' - T_e'') + [G(v') - G(v'')] + [F_{v'}(J') - F_{v''}(J'')] = \upsilon_e + \upsilon_{vib} + \upsilon_{rot}. \tag{2.15}$$

For different isotopic molecules (that is, molecules, whose atoms may differ in mass, but whose nuclei have identical atomic number,) the vibrational constants are different,

$$\omega_e^{\,i} = \rho^i \omega_e, \quad \omega_e^{\,i}\chi_e^{\,i} = (\rho^i)^2 \omega_e \chi_e, \quad \omega_e^{\,i} y_e^{\,i} = (\rho^i)^3 \omega_e y_e, \cdots \tag{2.16}$$

where $\rho^i = (\mu/\mu_i)^{1/2}$ and μ and μ_i are reduced masses of the two different isotopic molecules.

Then we get the vibrational shift between the two isotopic molecules,

$$\begin{aligned}\Delta\upsilon_{vib} = \upsilon_{vib} - \upsilon_{vib}^{\,i} &= (1-\rho^i)[\omega_e'(v'+\frac{1}{2}) - \omega_e''(v''+\frac{1}{2})] \\ &\quad - (1-\rho^{i^2})[\omega_e'\chi_e'(v'+\frac{1}{2})^2 - \omega_e''\chi_e''(v''+\frac{1}{2})^2] + \cdots.\end{aligned} \tag{2.17}$$

2.2 Rotational Structure

In the expression

$$\upsilon = \upsilon_e + \upsilon_{vib} + \upsilon_{rot}, \tag{2.18}$$

the quantity $\upsilon_0 = \upsilon_e + \upsilon_{vib}$ is a constant for a specific vibrational transition and called the band origin or the zero line while υ_{rot} is variable and depends on the different values of the rotational quantum number in the upper and lower states. We have

$$\upsilon = \upsilon_0 + \upsilon_{rot} = \upsilon_0 + [F_{v'}(J') - F_{v''}(J'')] = \upsilon_0 + B_{v'}J'(J'+1) - D_{v'}J'^2(J'+1)^2 + \ldots - [B_{v''}J''(J''+1) - D_{v''}J''^2(J''+1)^2 + \ldots], \quad (2.19)$$

where $F_{v'}(J')$ and $F_{v''}(J'')$ are the rotational terms of the upper and lower state, respectively.

2.2.1 Selection Rules and the Branches of a Band

If at least one of the two states has $\Lambda \neq 0$ (Λ is the electronic angular momentum), the selection rule for J is

$$\Delta J = J' - J'' = 0, \quad \pm 1. \quad (2.20)$$

If $\Lambda = 0$ in both electronic states, the selection rule for J is

$$\Delta J = J' - J'' = \pm 1. \quad (2.21)$$

Thus we will have three or two series of branches, respectively,

$$\begin{aligned} &\text{R branch}: \quad \upsilon = \upsilon_0 + [F_{v'}(J+1) - F_{v''}(J)] = R(J) \quad \text{with } \Delta J = +1, \\ &\text{Q branch}: \quad \upsilon = \upsilon_0 + [F_{v'}(J) - F_{v''}(J)] = Q(J) \quad \text{with } \Delta J = 0, \\ &\text{P branch}: \quad \upsilon = \upsilon_0 + [F_{v'}(J-1) - F_{v''}(J)] = P(J) \quad \text{with } \Delta J = -1. \end{aligned} \quad (2.22)$$

Where J's are the rotational quantum numbers in the lower state ($= J''$).

Substitute Eq. (2.8) into Eq. (2.22) and neglect the small correction term in D_v, we get

$$\begin{aligned}
&\text{R branch}: \quad \upsilon = \upsilon_0 + 2B_{v'} + (3B_{v'} - B_{v''})J + (B_{v'} - B_{v''})J^2 = R(J),\\
&\text{Q branch}: \quad \upsilon = \upsilon_0 \qquad\quad + (B_{v'} - B_{v''})J + (B_{v'} - B_{v''})J^2 = Q(J),\\
&\text{P branch}: \quad \upsilon = \upsilon_0 \qquad\quad - (B_{v'} + B_{v''})J + (B_{v'} - B_{v''})J^2 = P(J). \qquad (2.23)
\end{aligned}$$

The P and R branches can be presented by a single formula,

$$\upsilon = \upsilon_0 + (B_{v'} + B_{v''})m + (B_{v'} - B_{v''})m^2, \qquad (2.24)$$

where m = -J for the P branch and $m = J + 1$ for the R branch.

Using Eq. (2.23) for a given band origin υ_0, that is, within one vibrational component, we can calculate spacings between lines in the branches

$$\begin{aligned}
&\Delta\upsilon_R(J) = \upsilon_R(J+1) - \upsilon_R(J) = 2(B_{v'} - B_{v''})J + 2(2B_{v'} - B_{v''}),\\
&\Delta\upsilon_Q(J) = \upsilon_Q(J+1) - \upsilon_Q(J) = 2(B_{v'} - B_{v''})J + 2(B_{v'} - B_{v''}),\\
&\Delta\upsilon_P(J) = \upsilon_P(J+1) - \upsilon_P(J) = 2(B_{v'} - B_{v''})J - 2B_{v''}. \qquad (2.25)
\end{aligned}$$

Plotting spacings $\Delta\upsilon$ against J obtained from an experiment, one can determine $B_{v'}$ and $B_{v''}$ from the slope of the plot and its intercept with the vertical axis, respectively.

Furthermore, we have the combination relations[19] (page 183)

$$\begin{aligned}
&\Delta_1F'(J) = R(J) - Q(J) \qquad = F_{v'}(J+1) - F_{v'}(J),\\
&\Delta_1F'(J) = Q(J+1) - P(J+1) = F_{v'}(J+1) - F_{v'}(J),\\
&\Delta_1F''(J) = R(J) - Q(J+1) \qquad = F_{v''}(J+1) - F_{v''}(J),\\
&\Delta_1F''(J) = Q(J) - P(J+1) \qquad = F_{v''}(J+1) - F_{v''}(J). \qquad (2.26)
\end{aligned}$$

From these combination differences we obtain the separation $\Delta_1F(J)$ of successive rotational levels. Substitute Eq. (2.8) in $\Delta_1F(J)$ and neglect the small correction term in D_v, we get

$$\Delta_1 F(J) = F_v(J+1) - F_v(J) = 2B_v(J+1). \tag{2.27}$$

If a Q branch is not presented, we have[19] (page 177)

$$\begin{aligned} \Delta_2 F'(J) &= R(J) - P(J) \quad = F_{v'}(J+1) - F_{v'}(J-1), \\ \Delta_2 F''(J) &= R(J-1) - P(J+1) = F_{v''}(J+1) - F_{v''}(J-1), \end{aligned} \tag{2.28}$$

and

$$\Delta_2 F(J) = F_v(J+1) - F_v(J-1) = 4B_v(J+\frac{1}{2}). \tag{2.29}$$

B_v values then can be obtained from the slope of $\Delta_1 F(J)$ or $\Delta_2 F(J)$ plots.

2.2.2 Intensity Distribution in the Rotational Structure

According to quantum theory, each state of an atomic system with total angular momentum J consists of $2J+1$ levels. Assuming a Boltzmann distribution, the number of molecules N_J in the rotational level J can be given by[19] (page 125)

$$N_J = \frac{N_v}{Q_r}(2J+1)e^{-hcB_v J(J+1)/kT}, \tag{2.30}$$

where N_v is the total number of molecules in the vibrational level v, and Q_r is the rotational state sum

$$Q_r = \sum_J (2J+1)e^{-hcB_v J(J+1)/kT}. \tag{2.31}$$

Thus the maximum of intensity occurs in each branch at[19] (page 124)

$$J_{\max.} = \sqrt{\frac{kT}{2Bhc}} - \frac{1}{2} = 0.5896\sqrt{\frac{T}{B}} - \frac{1}{2}. \qquad (2.32)$$

2.3 Coupling of Rotation and Electronic Motion

In order to describe the electronic motion in the field of two fixed nuclei, it is necessary to take into consideration the fact that the actual rotation and vibration of nuclei in a molecule take place simultaneously with the motion of electrons, and these different motions influence one another.

The mutual interactions between vibrational and electronic motions and the rotational and vibrational motions have been taken into account in the Schrödinger Eq. (2.3) and (2.4), respectively. Since the vibrational levels are chosen to fit the potential curve that represents the dependence of the electronic energy on the internuclear distance. Now we need to consider the influence of rotational and electronic motions on each other; that is, we must find out by what quantum numbers we can describe the rotational levels in the different types of electronic states, how their energies depend on these quantum numbers, and what symmetry properties the corresponding eigenfuntions possess.

The different angular momenta in the molecule — electron spin $\boldsymbol{S}$, electronic orbital angular momentum $\boldsymbol{L}$, angular momentum of nuclear rotation $\boldsymbol{R}$ — form the total angular momentum $\boldsymbol{J}$. The character of the coupling is determined by three types of interaction in a molecule: between $\boldsymbol{L}$ and the internuclear axis (that is, the line joining the nuclei) that represents the electrostatistic field produced by the two nuclear charges, between $\boldsymbol{L}$ and $\boldsymbol{S}$, and between total electronic angular momentum $\boldsymbol{\Omega}$ and $\mathbf{R}$. $\boldsymbol{\Omega}$ is obtained by adding $\boldsymbol{\Lambda}$ and $\boldsymbol{\Sigma}$,

where $\mathbf{\Lambda}$ and $\mathbf{\Sigma}$ are the components of $\boldsymbol{L}$ and $\boldsymbol{S}$ momenta along the internuclear axis, respectively.

2.3.1 Orbital Angular Momentum, Spin and Total Angular Momentum of the Electrons

A precession of $\boldsymbol{L}$ takes place about the internuclear axis with constant component M_L ($h/2\pi$), where M_L can take the values

$$M_L = L, L-1, L-2, \cdots, -L. \tag{2.33}$$

Then we have

$$\Lambda = |M_L| = 0, 1, 2, \cdots, L. \tag{2.34}$$

See Fig. II-1. According as Λ = 0, 1, 2, 3, …, the corresponding molecular state is designated a Σ, Π, Δ, Φ, … state. Π, Δ, Φ, … states are doubly degenerate since M_L have two values $+\Lambda$ and $-\Lambda$; Σ states are non-degenerate.

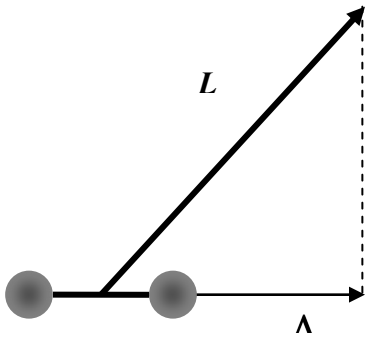

Figure II-1. Precession of the orbital angular momentum $\boldsymbol{L}$ about the internuclear axis.

If $\Lambda \neq 0$, there is an internal magnetic field in the direction of the internuclear axis resulting from the orbital motion of the electrons. This magnetic field causes a precession of $\boldsymbol{S}$ about the field axis with a constant component M_S ($h/2\pi$). For molecules, M_S is denoted by Σ. The values of Σ are

$$\Sigma = S, S-1, S-2, \cdots, -S. \tag{2.35}$$

The total electronic angular momentum about the internuclear axis $\boldsymbol{\Omega}$ is obtained by adding $\boldsymbol{\Lambda}$ and $\boldsymbol{\Sigma}$. Since $\boldsymbol{\Lambda}$ and $\boldsymbol{\Sigma}$ both lie along the internuclear axis, we have

$$\Omega = |\Lambda + \Sigma|. \tag{2.36}$$

2.3.2 Hund's Coupling Cases

The classification of different modes of coupling was first done by Hund.[23]

2.3.2.1 Hund's Case (a)

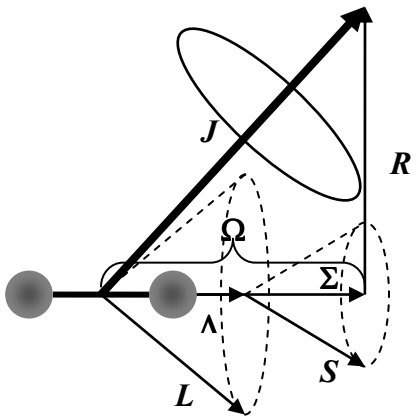

Figure II-2. Vector diagram for Hund's case (a). Solid-line ellipse represents the nutation of $\boldsymbol{J}$ while the much more rapid presessions of $\boldsymbol{L}$ and $\boldsymbol{S}$ are indicated by the broken-line ellipses.

In this case, the interaction of the rotation with the electronic motion is very weak whereas the electronic motion itself is coupled very strongly to the internuclear axis. The electronic angular momentum $\boldsymbol{\Omega}$ is then well defined. $\boldsymbol{\Omega}$ and the angular momentum $\boldsymbol{R}$ of nuclear rotation form the resultant $\boldsymbol{J}$. Fig. II-2 gives the vector diagram for this case.

The rotational energy in Hund's case (a) is, neglecting centrifugal stretching term,

$$F_v(J) = B_v J(J+1) - \Omega^2, \tag{2.37}$$

where

$$J = \Omega, \Omega+1, \Omega+2, \cdots. \tag{2.38}$$

For a given multiplet term B_v has the same value for each multiplet component except when the multiplet splitting is very large.

2.3.2.2 Hund's Case (b)

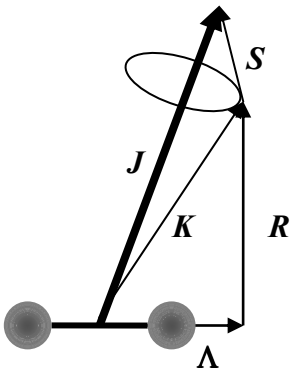

Figure II-3. Vector diagram for Hund's case (b). ***K*** and ***S*** rotate about the direction of ***J***. For Λ=0, ***K***(≡***R***) is perpendicular to the internuclear axis.

When $\Lambda = 0$ and $S \neq 0$, the spin vector $\boldsymbol{S}$ is not coupled to the internuclear axis at all, which means that $\boldsymbol{\Omega}$ is undefined. Thus Hund's case (a) cannot apply. Sometimes, particularly for light molecules, even if $\Lambda \neq 0$, S may be only very weakly coupled to the internuclear axis. See Fig. II-3.

The angular momenta $\boldsymbol{\Lambda}$ and $\boldsymbol{R}$ form a resultant $\boldsymbol{K}$ which is the total angular momentum apart from spin. We have

$$K = \Lambda, \Lambda + 1, \Lambda + 2, \cdots. \tag{2.39}$$

$\boldsymbol{J}$ is the total angular momentum including spin and is formed by the angular momenta $\boldsymbol{K}$ and $\boldsymbol{S}$,

$$J = (K + S), (K + S - 1), (K + S - 2), \cdots, |K - S|. \tag{2.40}$$

2.3.2.3 Hund's Case (c)

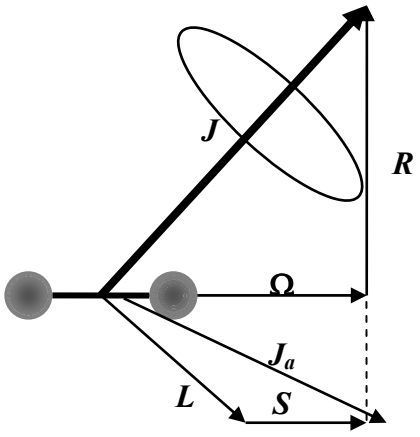

Figure II-4. Vector diagram for Hund's case (c). Solid-line ellipse represents the nutation of $\boldsymbol{J}$.

The interaction between $\boldsymbol{L}$ and $\boldsymbol{S}$, in certain cases, particularly for heavy molecules, may be stronger than the interaction with the internuclear axis. In this case Λ and Σ are not defined. $\boldsymbol{L}$ and $\boldsymbol{S}$ first form a resultant $\boldsymbol{J}_a$ which is then coupled to the internuclear axis with a component Ω. The electronic angular momentum $\boldsymbol{\Omega}$ and the angular momentum $\boldsymbol{R}$ of nuclear rotation then form the resultant angular momentum $\boldsymbol{J}$ just as in case (a). Fig. II-4 gives the vector diagram for this case. The rotational energy levels and their $\boldsymbol{J}$ values are given by the same formulae (2.37) and (2.38) as for case (a).

2.4 Symmetry Properties of the Rotational Levels and the Selection Rules

The complete eigenfunctions of a molecule (excluding the electron and nuclear spin), to a first approximation, is a product of an electronic (ψ_e), a vibrational (ψ_v), and a rotational (ψ_r) contribution

$$\psi = \psi_e \frac{1}{r} \psi_v \psi_r . \tag{2.41}$$

The rotational levels of a diatomic molecule are classified according to the behavior of the total eigenfunction (not of the rotational eigenfunction alone).

A rotational level is called positive or negative depending on whether the total eigenfunction remains unchanged or changes sign with respect to a reflection at the origin. The property positive or negative is also called parity.

For homonuclear molecule, the total eigenfunction either remains unchanged or only changes its sign for an exchange of the nuclei. The rotational level is called symmetric or antisymmetric in the nuclei according as the former or the latter is the case.

Since the vibrational contribution $(1/r)\psi_v$ depends only on the magnitude of the internuclear distance, it always remains unchanged for the above two actions. If we designate the total angular momentum apart from spin by *K*, the rotational wave functions with even *K* are positive and symmetric while those with odd *K* are negative and antisymmetric.

2.4.1 Symmetry Properties of the Electronic Eigenfunctions

In a diatomic molecule any plane through the internuclear axis is a plane of symmetry. Therefore the electronic eigenfuntion ψ_e of a non-degenerate state (Σ state) either remains unchanged or changes sign when reflected at any plane passing through both nuclei. Then the state is called a Σ^+ or a Σ^- state, respectively. For degenerate states (Π, Δ, Φ, …states), the situation is more complicated. However, linear combinations of eigenfunction can easily be found such as remain unchanged or change into their negatives by the reflection. We may therefore also distinguish Π^+, Π^-, Δ^+, Δ^-, … states.

If the two nuclei in the molecule have the same charge, in addition to the symmetry axis, the molecule has a center of symmetry. Then the electronic eigenfuntions remain either unchanged or only change sign when reflected at the center. In the first case, the state to which the eigenfunction belongs is called an even state while in the second case an odd state. The symmetry property even or odd is indicated by adding a subscript *g* or *u*, respectively, to the term symbol (from the German “gerade” and “ungerade”).

The symmetry properties of the rotational levels are influenced by the symmetry of the electronic eigenfuntions.

An inversion of the total wavefunction is equivalent to a rotation of the molecule through 180° about an axis perpendicular to the internuclear axis, followed by a reflection at a plane perpendicular to this rotational axis and passing through the internuclear axis. Since ψ_e depends only on the co-ordinates of the electrons relative to the nuclei and the internuclear distance, it is not influenced by the first operation. The second operation defines the symmetry property positive or negative of the electronic eigenfunction ψ_e. An exchange of the nuclei is equivalent to an inversion of the total wavefunction followed by an inversion of only the electronic eigenfunction which defines the symmetry property even or odd of the electronic eigenfunction. Thus the electronic state Σ_g^+ is symmetric while Σ_u^+ antisymmetric.

2.4.2 Selection Rules

For any atomic system the selection rule for the quantum number J of the total angular momentum is

$$\Delta J = 0, \quad \pm 1, \text{ with the restriction } J = 0 \not\rightarrow J = 0. \tag{2.42}$$

We also have the symmetry selection rules: positive terms combine only with negative, and vice versa

$$+ \leftrightarrow -, \quad + \not\leftrightarrow +, \quad - \not\leftrightarrow -; \tag{2.43}$$

and for identical nuclei, symmetric terms combine only with symmetric and antisymmetric only antisymmetric,

$$s \leftrightarrow s, \quad a \leftrightarrow a, \quad s \not\leftrightarrow a. \tag{2.44}$$

In the case of a molecule with nuclei of equal charge, we also have the selection rule that even electronic states combine only with odd,

$$g \leftrightarrow u, \quad g \not\leftrightarrow g, \quad u \not\leftrightarrow u. \tag{2.45}$$

2.4.2.1 Selection Rules Holding for Hund's Case (a) and (b)

In Hund's case (a) and (b), the quantum number Λ is defined and we have

$$\Delta\Lambda = 0, \quad \pm 1. \tag{2.46}$$

We also have

$$\Sigma^+ \leftrightarrow \Sigma^+, \quad \Sigma^- \leftrightarrow \Sigma^-, \quad \Sigma^+ \not\leftrightarrow \Sigma^-. \tag{2.47}$$

In case (a) and (b) the resultant spin $\boldsymbol{S}$ is defined, and for the corresponding quantum number there is the selection rule

$$\Delta S = 0. \tag{2.48}$$

This means that only states of the same multiplicity combine with one another. This prohibition of intercombinations holds less and less rigorously with increasing interaction of $\boldsymbol{S}$ and $\boldsymbol{\Lambda}$, that is, with increasing nuclear charge.

2.4.2.2 Selection Rules Holding only in Hund's Case (a)

In Hund's case (a), the quantum number Σ of the component of the spin in the internuclear axis is defined and we have

$$\Delta\Sigma = 0. \tag{2.49}$$

And we also have

$$\Delta\Omega = 0, \quad \pm 1. \tag{2.50}$$

If Ω=0 for both electronic states, we have

$$\Delta J = 0 \text{ is forbidden for } \Omega = 0 \rightarrow \Omega = 0. \tag{2.51}$$

2.4.2.3 Selection Rules Holding only in Hund's Case (b)

In Hund's case (b), the quantum number K of the total angular momentum apart from spin is defined. We have

$$\Delta K = 0, \quad \pm 1 \tag{2.52}$$

with the restriction

$$\Delta K = 0 \text{ is forbidden for } \Sigma - \Sigma \text{ transitions.} \tag{2.53}$$

2.4.2.4 Selection Rules Holding only in Hund's Case (c)

In Hund's case (c), apart from $\boldsymbol{J}$ only the quantum number Ω of the total electronic angular momentum about the internuclear axis is well defined. We have

$$\Delta\Omega = 0, \quad \pm 1. \tag{2.54}$$

In addition, we have

$$0^+ \leftrightarrow 0^+, \quad 0^- \leftrightarrow 0^-, \quad 0^+ \not\leftrightarrow 0^-. \tag{2.55}$$

The special selection rules discussed above hold only if both participating states belong to one and the same coupling case. If the two states belong to two different coupling cases, these special selection rules lose their validity and there remain only the selection rules holding for both coupling cases.

2.5 Mercury Dimers and the $D1_u \leftarrow X0^+_g$ Transition

2.5.1 Mercury Isotopes

Mercury with natural isotopic abundance contains seven stable isotopes. See Table II-1. The resulting dimers then consist of 28 isotopomers (isotopic molecules) with 15 distinct total mass numbers as listed in Table II-2.

In Table II-2, A_1 and A_2 are the mass numbers of the mercury isotopes while $^{A_1}\mathrm{Hg}\,^{A_2}\mathrm{Hg}$ are the isotopomers formed by the isotopes $^{A_1}\mathrm{Hg}$ and $^{A_2}\mathrm{Hg}$ with individual nuclear spin I_1 and I_2. The total mass number and the reduced mass of the isotompomer are $A_1 + A_2$ and μ_i, respectively. The total abundances of the isotopomers with the same mass number are the sum of the individual abundances of the corresponding isotopomers. According to Eq. (2.17), each vibrational band of the mercury dimer will then consist of 15 subbands correspond to the 15 distinct dimer mass numbers and in each subband there are also shifts between the transition frequencies of different combinations.

Table II-1. Naturally occurring mercury isotopes.

Isotope	Atomic mass	Natural abundance (%)	Nuclear spin
^{196}Hg	195.965807(5)	0.15	0
^{198}Hg	197.966743(4)	9.97	0
^{199}Hg	198.968254(4)	16.87	1/2
^{200}Hg	199.968300(4)	23.10	0
^{201}Hg	200.970277(4)	13.18	3/2
^{202}Hg	201.970617(4)	29.86	0
^{204}Hg	203.973467(5)	6.87	0

Table II-2. $^{A_1}Hg\,^{A_2}Hg$ isotopomers formed by seven stable isotopes.

A_1	A_2	A_1+A_2	I_1	I_2	μ_i	Individual abundances	Total abundances
196	196	392	0	0	97.983	0.0002%	0.0002%
196	198	394	0	0	98.481	0.0299%	0.0299%
196	199	395	0	1/2	98.728	0.0506%	0.0506%
196	200	396	0	0	98.973	0.0693%	1.0633%
198	198		0	0	98.983	0.9940%	
196	201	397	0	3/2	99.183	0.0395%	3.4034%
198	199		0	1/2	99.233	3.3639%	
196	202	398	0	0	99.461	0.0896%	7.5417%
198	200		0	0	99.481	4.6061%	
199	199		1/2	1/2	99.484	2.8460%	
198	201	399	0	3/2	99.728	2.6281%	10.4220%
199	200		1/2	0	99.733	7.7939%	
196	204	400	0	0	99.945	0.0206%	15.7577%
198	202		0	0	99.974	5.9541%	
199	201		1/2	3/2	99.982	4.4469%	
200	200		0	0	99.984	5.3361%	
199	202	401	1/2	0	100.229	10.0748%	16.1639%
200	201		0	3/2	100.234	6.0892%	
198	204	402	0	0	100.462	1.3699%	16.9023%
200	202		0	0	100.482	13.7953%	
201	201		3/2	3/2	100.485	1.7371%	
199	204	403	1/2	0	100.720	2.3179%	10.1890%
201	202		3/2	0	100.734	7.8711%	
200	204	404	0	0	100.975	3.1739%	12.0901%
202	202		0	0	100.985	8.9162%	
201	204	405	3/2	0	101.230	1.8109%	1.8109%
202	204	406	0	0	101.483	4.1028%	4.1028%
204	204	408	0	0	101.987	0.4720%	0.4720%

2.5.2 Forbidden Electronic Transition $D^3\Sigma_u^+(1_u) \leftarrow X^1\Sigma_g^+(0_g^+)$

Under certain conditions, transitions occur that contradict the selection rules discussed in section 2.4. They are called the forbidden transitions. The transition $D^3\Sigma_u^+(1_u) \leftarrow X^1\Sigma_g^+(0_g^+)$ is a singlet-triplet transition which is principally forbidden. But it can be observed for heavy molecules, such as Hg_2, because the strong spin-orbit interaction causes the $^3\Sigma$ state to have some of the properties of a $^1\Pi$ state.[19] (page 275) The rotational levels and their symmetries of states $X^1\Sigma_g^+(0_g^+)$ and $D^3\Sigma_u^+(1_u)$ are shown in Fig. II-5. For Hg_2 molecules, Hund's case (c) coupling is generally used in the transition analysis.

Since the electronic ground state $X^1\Sigma_g^+(0_g^+)$ is symmetric, rotational levels with even J'' are symmetric while odd J'' antisymmetric. For homonuclear isotopomers with nuclear spin $I_1=I_2=0$, the total nuclear spin I is zero and the nuclear spin wavefunction is symmetric. Since the system is a boson system, a symmetric total wavefunction is required to conform to the Pauli principle. Thus the antisymmetric rotational levels with odd J'' do not exist. For fermion system, the symmetric nuclear spin wavefunction is related to odd I while antisymmetric to even I. Thus the symmetric rotational levels with even J'' will be associated with even I while the antisymmetric rotational levels with odd J'' with odd I. For example, the two spin-1/2 nuclei of a $^{199}Hg^{199}Hg$ molecule form either a nuclear spin singlet (total nuclear spin $I=0$, antisymmetric) or spin triplet ($I=1$, symmetric). Thus for $^{199}Hg^{199}Hg$ molecule, in the ground state the nuclear singlet states are associated with even J'', and triplet states with odd J'', respectively. From Eq. (2.30), we can then obtain the

fractional population of the rotational level J for the $^{199}Hg^{199}Hg$ molecule in the ground state

$$\eta_J = \frac{N_J}{N_v} = \frac{1}{Q_r}(2J+1)e^{-hcB_vJ(J+1)/kT} \qquad \text{for even } J,$$
$$\eta_J = \frac{N_J}{N_v} = \frac{3}{Q_r}(2J+1)e^{-hcB_vJ(J+1)/kT} \qquad \text{for odd } J, \tag{2.56}$$

where

$$Q_r = \sum_{J=0,2,4,\ldots}^{\infty}(2J+1)e^{-hcB_vJ(J+1)/kT} + 3\sum_{J=1,3,5,\ldots}^{\infty}(2J+1)e^{-hcB_vJ(J+1)/kT}. \tag{2.57}$$

For $^1\Pi$ state, there is a two-fold degeneracy without rotation, Λ-type doubling (or Ω-type doubling if use Hund's case (c)). For each J value one component level is positive and the other is negative and the upper components form one series, the lower components another with slightly different effective B values. In each of these series, designated c and d, positive and negative levels alternate, as illustrated in Fig. II-5. We use the designation c-levels for a series of rotational levels in which the even levels are + and the odd – and the designation d-levels for a series in which the even levels are – and the odd +. Whether the c-levels or the d-levels lie higher depends on the position of neighboring Σ states. If there is only a Σ^+ state in the neighborhood, the c-levels is the upper (lower) one if the Σ^+ is below (above) the Π state.[19] (page 239) Now we have the rotational term

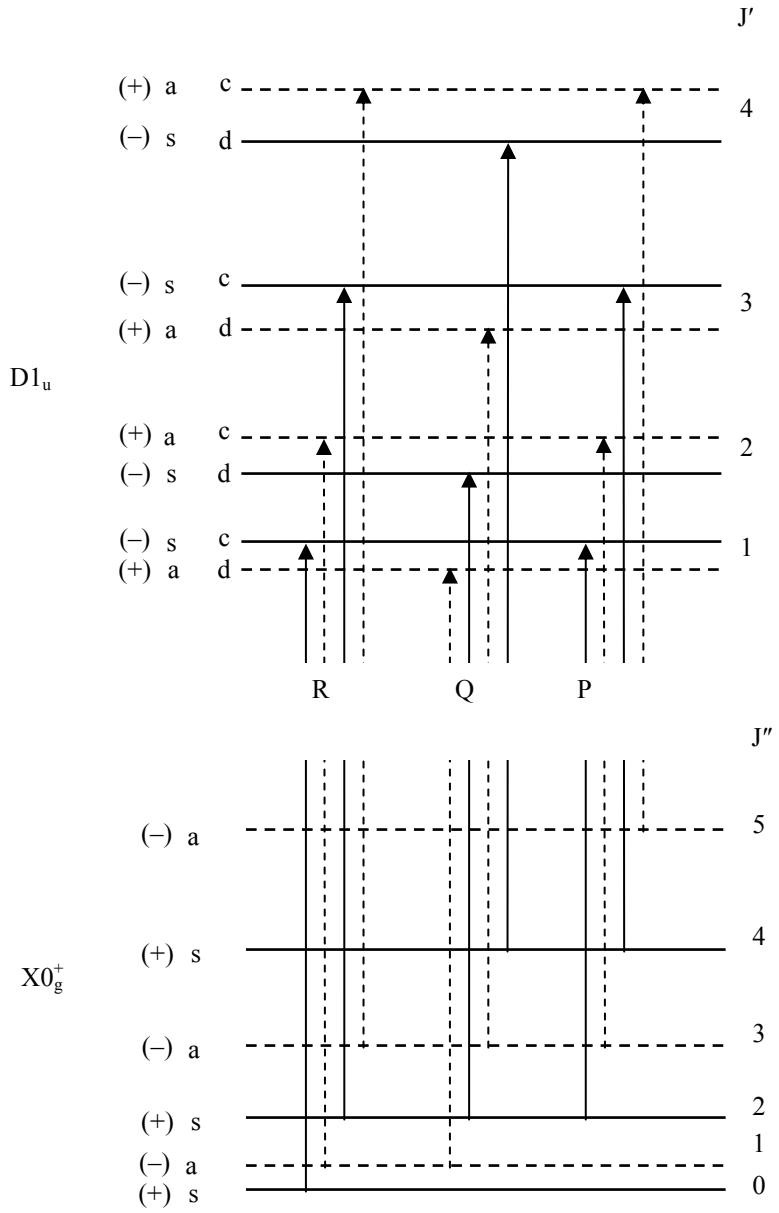

Figure II-5. Rotational levels in the transition $D^3\Sigma^+_u$ (1_u) ←$X^1\Sigma_g^+$ (0^+_g) and their symmetry properties. Broken lines represent antisymmetric rotational levels which do not exist for homonuclear isotopmers (A_1=A_2) with zero nuclear spin (I_1=I_2=0).

$$F_v^i(J) = B_v J(J+1) - D_v J^2(J+1)^2 + \cdots + \Phi_i(J), \tag{2.58}$$

where the subscript i stands for c or d. $\Phi_i(J)$ is a very small correction and may be represented by [19] (page 227)

$$\Phi_i(J) = \kappa_i + \delta_i J(J+1) + \mu_i J^2(J+1)^2 + \cdots, \tag{2.59}$$

Where $\mu_i << \delta_i$ and κ_i is of the order of magnitude of δ_i. If κ_i is neglected, we have

$$F_v^{\,i}(J) = B_v^{\,i} J(J+1) - D_v^{\,i} J^2(J+1)^2 + \cdots, \tag{2.60}$$

where $B_v^{\,i}$ and $D_v^{\,i}$ are effective B_v and D_v values,

$$\begin{aligned} B_v^{\,i} &= B_v + \delta_i, \\ D_v^{\,i} &= D_v + \mu_i. \end{aligned} \tag{2.61}$$

Thus the rotational levels of each of the substates c or d may be represented in exactly the same manner as those of the simple vibrating rotator.

Since the lines of the P and R branches now will always have a somewhat different upper state from the lines of the Q branch because of the selection rules (2.43) and (2.44), the combination relations Eq. (2.30) no longer hold exactly. We have a so-called combination defect,

$$\begin{aligned} \Delta_1 F'(J) &\approx R(J) - Q(J) = Q(J+1) - P(J+1) + \varepsilon, \\ \Delta_1 F''(J) &\approx R(J) - Q(J+1) = Q(J) - P(J+1) + \varepsilon, \end{aligned} \tag{2.62}$$

where the combination defect ε is equal to the sum of the Λ splitting of the terms with J and J+1. To a first good approximation, the Λ-type splitting is

$$\Delta\upsilon_v^{cd}(J) = F_v^{c}(J) - F_v^{d}(J) = qJ(J+1), \tag{2.63}$$

where

$$q = B_v^{c} - B_v^{d} = \delta_c - \delta_d . \tag{2.64}$$

CHAPTER III

DYE LASER EXPERIMENT

3.1 Experimental Setup

The experimental setup is shown in Fig. III-1.

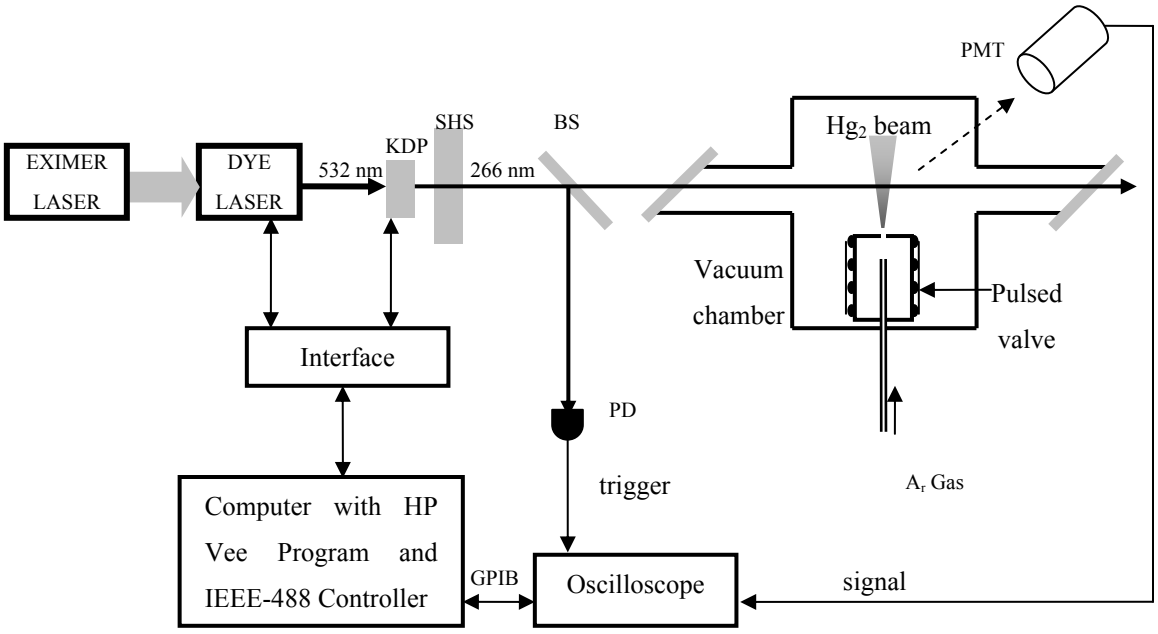

Figure III-1. Arrangement of the apparatus in the dye laser experiment: KDP: second harmonic crystal; SHS: second harmonic separator (Pellin-Broca prism set); BS: beam splitter; PD: photodiode; PMT: photomultiplier.

A free-jet expansion beam of Hg_2 was produced in a vacuum chamber evacuated by a 2400-ℓ/s oil-diffusion pump (Varian, Model VHS-6) backed up by a mechanical pump (Welch Duo-Seal, Model 1397). The stainless steel source of the molecular beam consisted of a high-temperature pulsed valve (General Valve, Series 9) whose orifice diameter *D* was 0.5 mm or 1 mm, and a mercury reservoir. The source was mounted in a cylindrical stainless steel tube allowing a horizontal translation of the source in the chamber and easy

adjustment of an effective distance (X_{eff}) from the valve orifice to the laser-beam interaction region (in the experiment, the range of X_{eff} varied from 8 mm to 12 mm). The valve was driven with an Iota One driver (Parker Instrumentation). Typical duration of the valve pulse was 1–2 ms. The laser pulse was delayed with respect to the valve pulse by about 1.5-2 ms. The dependence of the laser-induced fluorescence (LIF) signal on the delay between the valve pulse and the laser pulse was a main criterion for satisfactory excitation of Hg_2 in the beam.

Four separate heaters (Watlow) provided an independent adjustment of the temperature of the valve (510 K), connecting pipes (500 K) and Mercury reservoir (T_0=490 K). This assured a sufficient temperature difference between the valve and the reservoir, and prevented condensation of mercury vapors in the valve chamber and an eventual obstruction of its poppet armature. Ar was used as carry gas with pressures, p_{Ar}, from 10 psi to 20 psi. The stainless steel source parts that were in contact with the vacuum chamber walls were separated from the heated valve by a Macor ceramic disk. This beam source provided stable operation from a base pressure of 2×10^{-6} Torr with the beam off to a pressure 2×10^{-2} Torr (for p_{Ar}=10 psi) with the beam on.

The molecules in the supersonic beam were irradiated with a laser beam from a frequency doubled (KDP crystal) XeCl excimer laser (EMG 201-204 MSG, Lambda Physik) - pumped - dye laser (FL 3002E, Lambda Physik) utilizing coumarine 540 (Exciton). Narrowing of the laser bandwidth Δ_{las} to approximately 0.06 cm^{-1} in UV was achieved using an angle tuned air-gap intracavity etalon whose free-spectral-range (FSR) was 1-$cm^{-1}$and finesse was 30. It was found that depending on the alignment of the laser, the

bandwidth varied from 0.04 cm^{-1} to 0.08 cm^{-1}. The smallest laser frequency step, 0.025 cm^{-1}, used in the experiment provided resolution of some, but not all, characteristic details of the rotational profiles. The molecular and laser beams were crossed in the interaction region at right angles to minimize residual Doppler broadening, Δ_{Dopp}. The latter was estimated to be less than 0.02 cm^{-1} for the 10°-divergence of the molecular beam and a molecular speed of 500 m/s. The fundamental laser frequency was calibrated against an iodine molecular spectrum and its bandwidth was frequently verified using an air-gap scanned Fabry-Perot interferometer (FSR=0.6 cm^{-1}).

The collection optics of the detection system consisted of a concave adjustable mirror placed inside the chamber below the interaction region, and a set of mirrors, quartz lenses and scattered-laser-light protective screens. The resulting total LIF emitted from the interaction region perpendicular to the direction of both molecular and laser beams was efficiently collected and focused on the photocathode of a photomultiplier (PM) tube (Amperex, Model 56DUVP). This detection system provided a possibility for optimization of the PM signal, while excluding undesired scattered light from the chamber. The recorded signal was normalized using the output from a photodiode that monitored the intensity of the second harmonic laser beam before it entered the vacuum chamber.

The T_v vibrational and T_r rotational temperatures of Hg_2 in the beam were estimated using a phenomenological formula for so-called translational temperature[24]:

$$T_T \approx \frac{T_0}{1+5896\left(p_{Ar}D\right)^{0.8}}, \tag{3.1}$$

where T_0, p_{Ar} and D are expressed in K, atm and cm, respectively. For the typical experimental parameters (*i.e.*, T_0 = 490 K, p_{Ar} = 10 psi (=0.68 atm) and D = 0.05 cm), Eq. (3.1) gives the $T_T \approx 1.5$ K. Using relations $T_r \approx T_T$ and $T_v \approx 10 \times T_r$ [25] we assume that T_r and T_v are 1.5 K and 15 K, respectively.

The intensity of the recorded LIF spectra depends on (1) the population of the ground-state J'' rotational levels in the v'' (which in turn depend on T_r, T_v, and the number of collisions, $\sim p_{Ar}D$, in the orifice); (2) the intensity of the laser radiation; (3) the electric dipole moment for the electronic transition (*i.e.*, $M(R)$[26]); (4) the Hönl-London factor for the rotational transition;[19] (page 208) (5) the Franck-Condon factor for the vibrational transition; and (6) the density of the species expanding in the beam. The density n_{eff} at the X_{eff} drops rapidly along the expansion according to the relationship[24]:

$$\frac{n_{eff}}{n_0} = \left[1 + \tfrac{1}{2}(\gamma - 1)M_{eff}^2\right]^{-1/(\gamma-1)}, \qquad (3.2)$$

where n_0 is density of Hg atoms in the source at T_0, $M_{eff}=3.26(X_{eff}/D)^{0.67}$ is an effective Mach number which characterizes the expansion at the X_{eff}, and γ is the heat capacity ratio c_p/c_v.[27] For typical experimental conditions (*i.e.*, $n_0=5\times10^{17}$ cm^{-3},[28] $X_{eff}=10$ mm and $D=1$ mm) $M_{eff}=15$ and n_{eff} drops by 3 orders of magnitude from the initial value.

3.2 Data Analysis

The $v'=57$ assignment in the $D1_u \leftarrow X0^+_g$ excitation spectrum was adopted from vibrational analysis of the excitation spectrum[25] which was previously recorded by Koperski *etal.*[29].

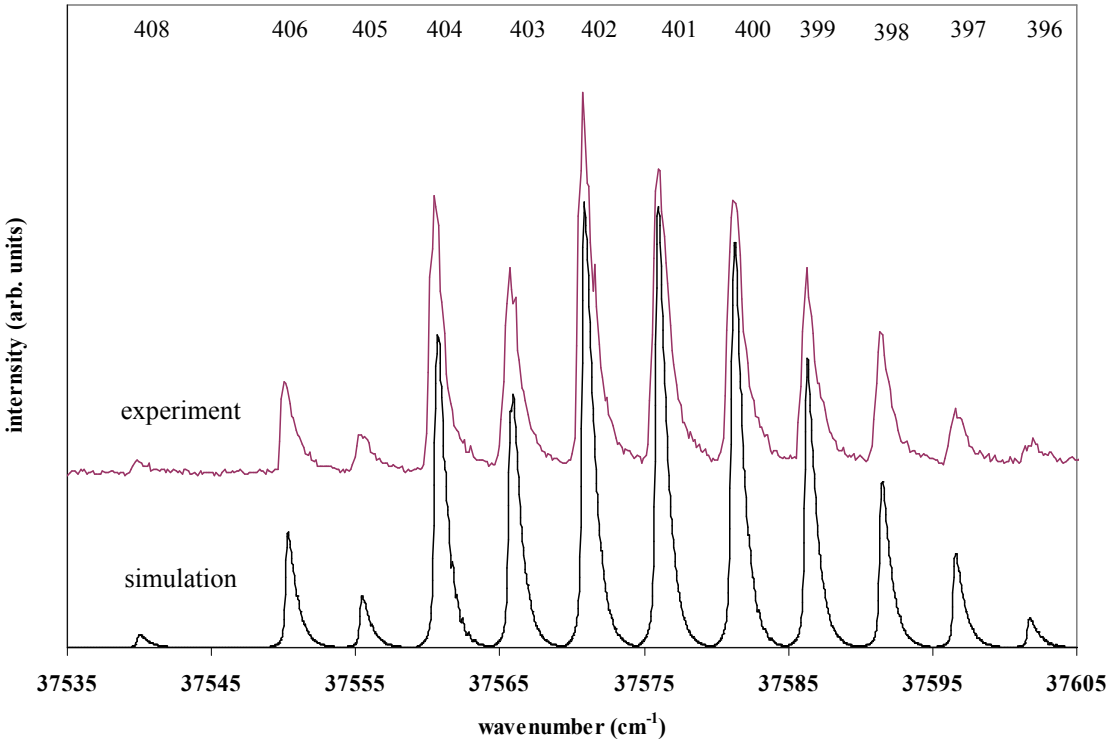

Figure III-2. Details of the (57, 0) vibrational band of the $D1_u \leftarrow X0_g^+$ transition recorded with a low laser resolution, D=1 mm, X_{eff}=12 mm, p_{Ar}=15 psi, T_0=465 K. Simulation taking into account the isotopic composition of the (57, 0) band and the rotational structure of all its isotopomers. Average values of $B_{v'=57}$ and $B_{v''=0}$ from Table III-1 as well as T_r=2 K and laser bandwidth Δ_{las}=0.17 cm^{-1} were used in the simulation. The A_1+A_2 are shown above corresponding components.

Fig. III-2 presents details of the (57, 0) vibrational band which was recorded with a low laser resolution (*i.e.*, without the intracavity etalon). The total isotopic composition of the (57, 0) consists of fifteen ^{A_1}Hg^{A_2}Hg components but in the experiment only twelve of them were sufficiently abundant to be observed. Among the A_1+A_2 combinations recorded in the experiment, the simplest, 405, 406 and 408 consisted of only one A_1+A_2 combination. Mass numbers 396, 397, 399, 401, 403 and 404 consisted of two A_1+A_2 combinations, 398 and 402 consisted of three A_1+A_2 combinations, and 404 consisted of four A_1+A_2

combinations. For all the components with more than one A_1+A_2 combination, the isotope shifts have an appreciable influence on the shape of their rotational profiles.

The simulations of the rotational spectra and the calculations of $B_{v'=57}$ and $B_{v''=0}$ were performed using a **PGOPHER** code.[30] **PGOPHER** is a flexible program which allows simulating and fitting of rotational spectra. It handles (1) linear molecules; (2) effects due to nuclear spin statistics and intensity alternation; (3) HF structure in homo- and heteronuclear isotopomers, and (4) many sorts of transitions, including forbidden transitions, such as the $^3\Sigma_u^+ \leftarrow {}^1\Sigma_g^+$ type. The program assumes a Boltzmann rotational levels population distribution. The simulation procedure was mainly focused on the reconstruction of the position of individual peaks corresponding to rotational transitions recorded in the experiment as well as the shape of the entire profile. However, it has to be taken into consideration that in a supersonic free-jet expansion beam the rotational-levels population distribution is governed by a non-Boltzmann function which ultimately, to some extent, modifies the shape of the rotational profile, especially for small J (*i.e.,* close to the bandhead).

In the simulation procedure, a simulation was first made with the experimental bandwidth Δ_{las} and Δ_{Dopp} (Δ_{las}=0.04-0.06 cm^{-1} and Δ_{Dopp}=0.02 cm^{-1}) using the initial values of $B_{v'=57}$ and $B_{v''=0}$ obtained previously (the Ω-type doubling was assumed to be very small, q_{Ω}~10^{-5}-10^{-6} cm^{-1},[31,32] without a noticeable influence on the simulated profiles). Then an approximate assignment of the recorded peaks to the R, P or Q branch was made and estimated values of $B_{v'=57}$ and $B_{v''=0}$ were determined using Eq. (2.25) –(2.29). The standard

deviations between the simulated and the experimental values of the position of individual peaks were calculated and minimized by repeating the above procedure. Ultimately, the best fit to the experimental profile resulted in a determination of the values of $B_{v'=57}$ and $B_{v''=0}$. To improve the fit, calculated $D_{v''=0}$ and $D_{v'=57}$ (Eq. (2.10), (2.12) and (2.14)) were introduced into the simulation program. Finally, the equilibrium R_e' and R_e'' rotational constants were determined (Eq. (2.9)) and ultimately, the R_e' and R_e'' bond lengths were calculated (Eq. (2.11)). The results were listed in Table III-1. The recorded and the simulated profiles of the 406, 404, 402, 400 and 398 components with all of their combinations were shown in Fig. III-3–Fig. III-7. The shape of the profile in Fig. III-4 is distinctively different from others because the dominating homonuclear isotopomer $^{202}Hg^{202}Hg$ represents a case of intensity alternation due to the spin statistics discussed in section 2.5.2.

From Eq. (2.32) with the constants in Table III-1, we can obtain the J values where the maximum of intensity occurs. For the component 398, J_{max} is 9. In the experimental realization of Bohm's spin-1/2 particle version of the EPR experiment, the $P(10)$ transition has been chosen since the nuclear singlet states in the electronic ground state of the $^{199}Hg^{199}Hg$ molecules are associated with even J''. The locations of the $P(10)$ transition and its adjacent transitions are indicated in Fig. III-8. However, the transition can not be resolved with the spectral resolution applied in this experiment and calls for an experiment with an ultra narrow-bandwidth excitation laser, alexandrite laser.

Table III-1. Rotational and vibrational characteristics of the $D1_u$ and $X0^+_g$ electronic states of Hg_2.

Designation	$D1_u$	$X0^+_g$
B_v	0.01788 [a,b] 0.01779 [a,c] 0.01770 [a,d] 0.01762 [a,e] 0.01753 [a,f] 0.0177±0.003 [g]	0.01295 [a,b] 0.01289 [a,c] 0.01285 [a,d] 0.01276 [a,e] 0.01270 [a,f]
B_e	0.02300 [b] 0.02288 [c] 0.02277 [d] 0.02266 [e] 0.02254 [f]	0.01305 [b] 0.01298 [c] 0.01291 [d] 0.01285 [e] 0.01279 [f] 0.0127±0.0003 [g]
R_e(Å)	2.715±0.010 [b-f] 2.5±0.1 [g] 2.83 [l]	3.605±0.010 [b-f] 3.63±0.04 [g] 3.73 [m]
ω_e	133±1 [h] 129.5±0.3 [i]	19.7±0.5 [g] 19±2 [h] 19.6±0.3 [j]
$\omega_e x_e$	0.52±0.02 [h] 0.50±0.01 [j]	0.27 [g] 0.26 [j] 0.26±0.03 [k]

All in [cm^{-1}] unless stated otherwise.

[a] for v'=57 of the $D1_u$ state and v''=0 of the $X0^+_g$ state;

[b-f] experimentally determined for $^{A_1+A_2}Hg_2$: [b] $^{398}Hg_2$, [c] $^{400}Hg_2$, [d] $^{402}Hg_2$, [e] $^{404}Hg_2$, [f] $^{406}Hg_2$;

[g] Ref.[33], (58,0) band, determined for the $^{202}Hg^{200}Hg$ isotopomer of the 402 component, see also [34];

[h] Ref. [35];

[i] Ref. [25];

[j] Ref. [29];

[k] Ref. [36];

[l] Ref. [26], *ab initio* value;

[m] Ref. [37], *ab initio* value.

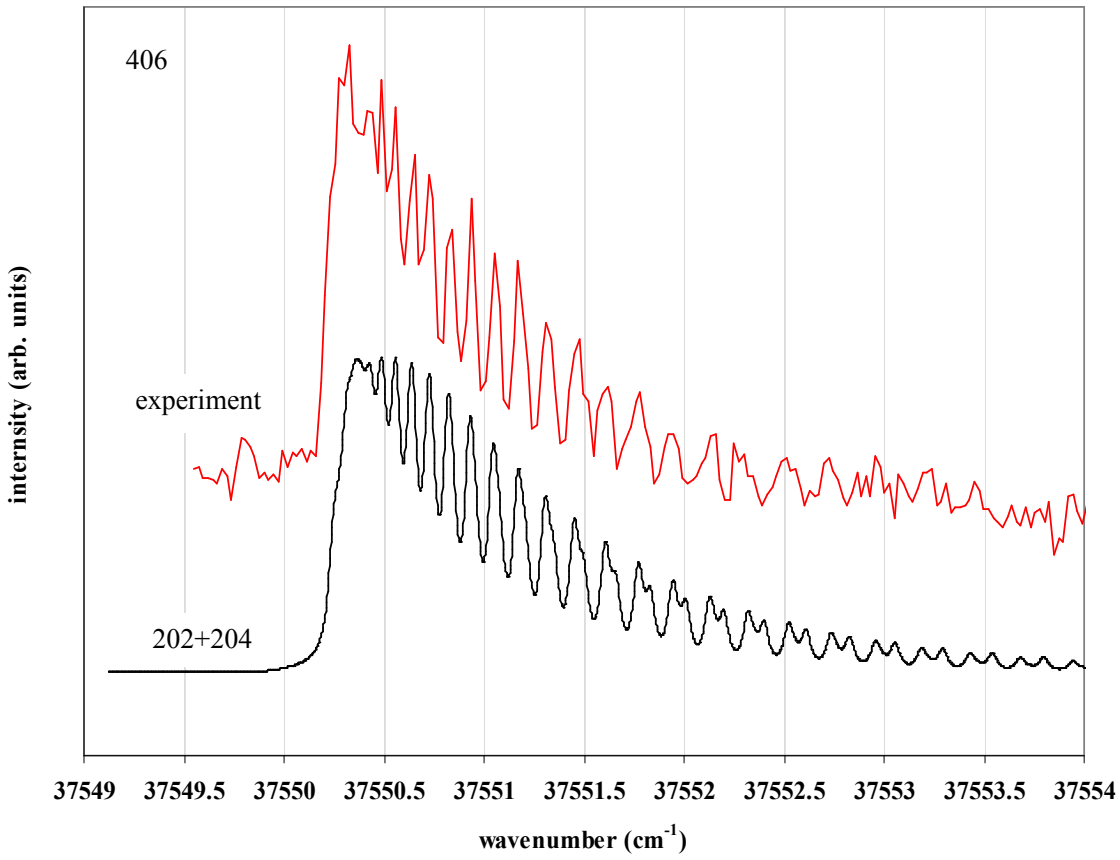

Figure III-3. The experimental and simulated profiles of the A_1+A_2=406 (^{202}Hg^{204}Hg) heteronuclear isotopomer of Hg_2. Simulation obtained for $B_{v'=57}$=0.01753 cm^{-1}, $B_{v''=0}$=0.01270 cm^{-1}, T_r=3.3 K, Δ_{Dopp}=0.02 cm^{-1} and Δ_{las}=0.05 cm^{-1}.

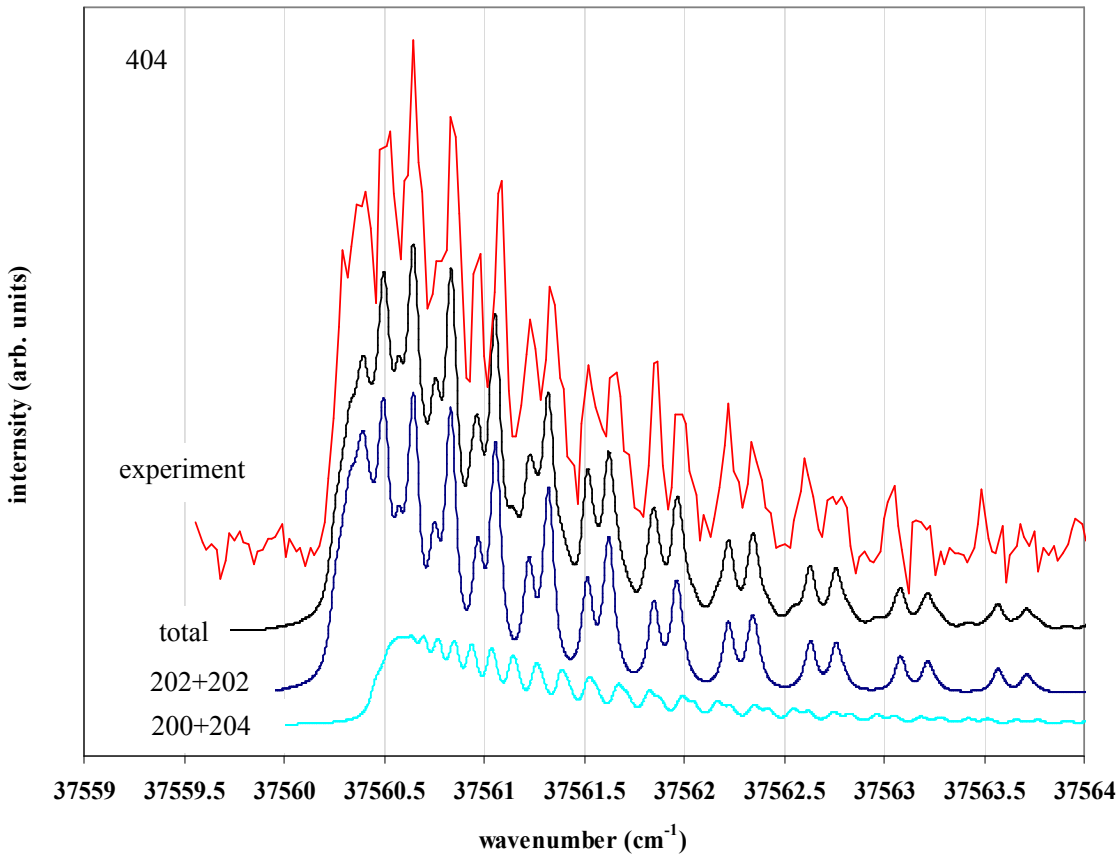

Figure III-4. The experimental and simulated profiles of the A_1+A_2=404 (^{202}Hg^{202}Hg and ^{200}Hg^{204}Hg) isotopic component of Hg_2. Simulation obtained for $B_{v'=57}$=0.01762 cm^{-1}, $B_{v''=0}$=0.01276 cm^{-1}, T_r=3.3 K, Δ_{Dopp}=0.02 cm^{-1} and Δ_{las}=0.06 cm^{-1}.

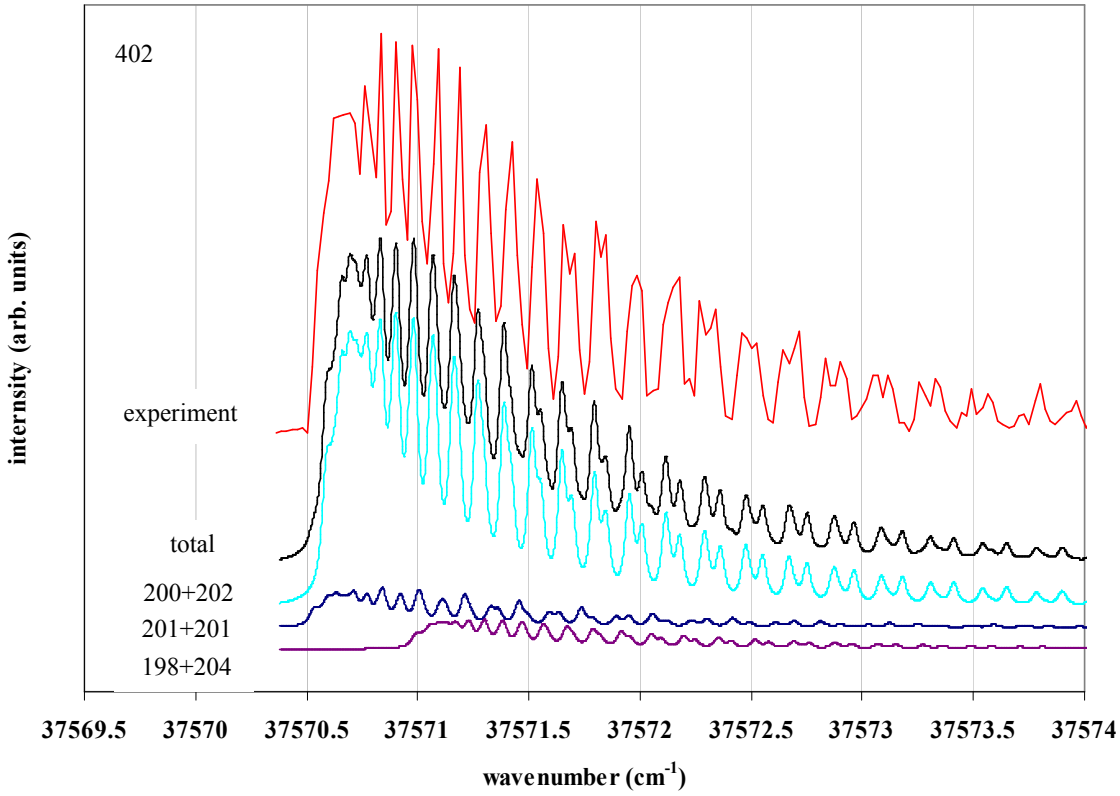

Figure III-5. The experimental and simulated profiles of the A_1+A_2=402 (^{200}Hg^{202}Hg, ^{201}Hg^{201}Hg and ^{198}Hg^{204}Hg) isotopic components of Hg_2. Simulation obtained for $B_{v'=57}$=0.01770 cm^{-1}, $B_{v''=0}$=0.01285 cm^{-1}, T_r=3.0 K, Δ_{Dopp}=0.015 cm^{-1} and Δ_{las}=0.038 cm^{-1}.

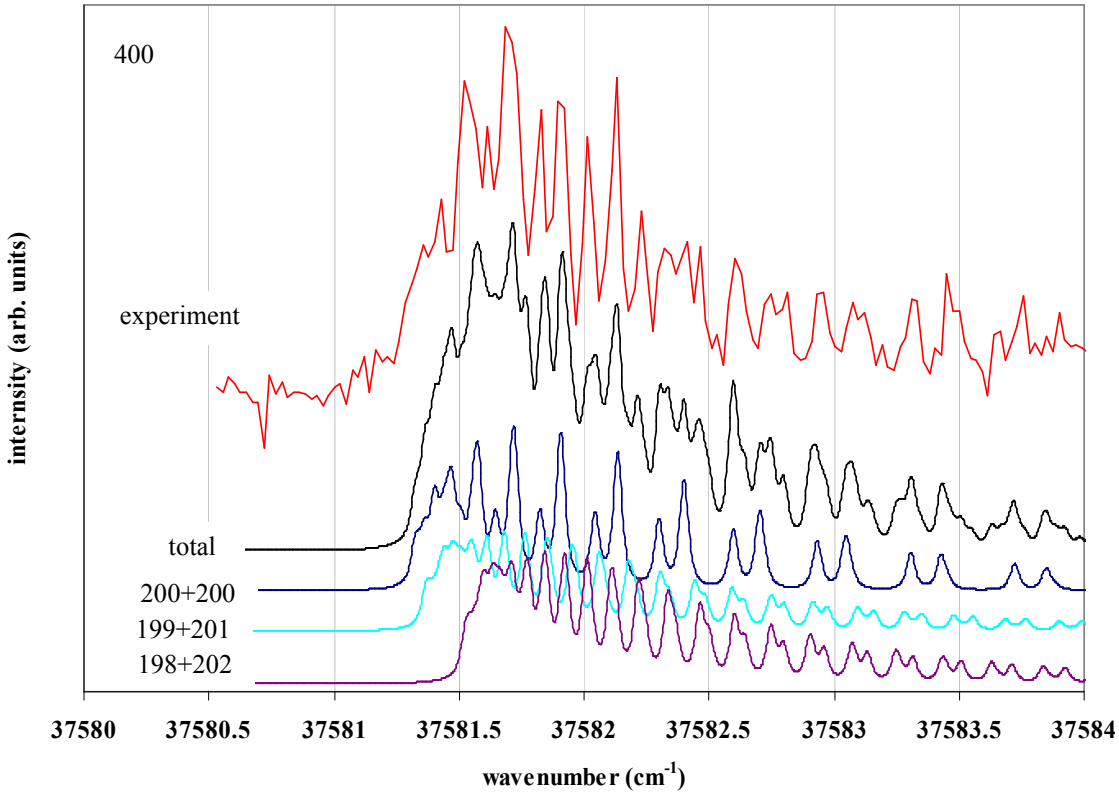

Figure III-6. The experimental and simulated profiles of the A_1+A_2=400 (^{198}Hg^{202}Hg, ^{199}Hg^{201}Hg, ^{200}Hg^{200}Hg and ^{196}Hg^{204}Hg) isotopic component of Hg_2. Simulation obtained for $B_{v'=57}$=0.01779 cm^{-1}, $B_{v''=0}$=0.01289 cm^{-1}, T_r=3.0 K, Δ_{Dopp}=0.02 cm^{-1} and Δ_{las}=0.033 cm^{-1}. Profile of the ^{196}Hg^{204}Hg isotopomer has too small an intensity to be visible.

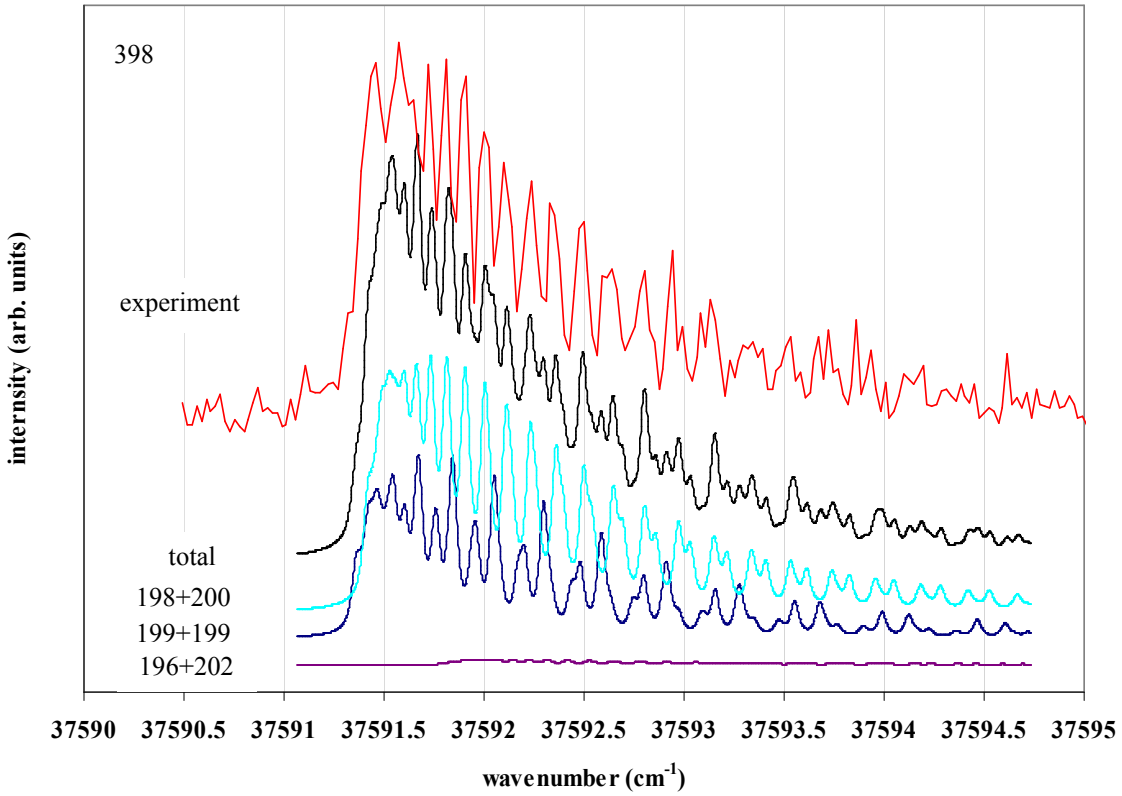

Figure III-7. The experimental and simulated profiles of the A_1+A_2=398 (^{198}Hg^{200}Hg, ^{199}Hg^{199}Hg and ^{196}Hg^{202}Hg) isotopic components of Hg_2. Simulations obtained for $B_{v'=57}$=0.01788 cm^{-1}, $B_{v''=0}$=0.01295 cm^{-1}, T_r=3.3 K, Δ_{Dopp}=0.02 cm^{-1} and Δ_{las}=0.04 cm^{-1}.

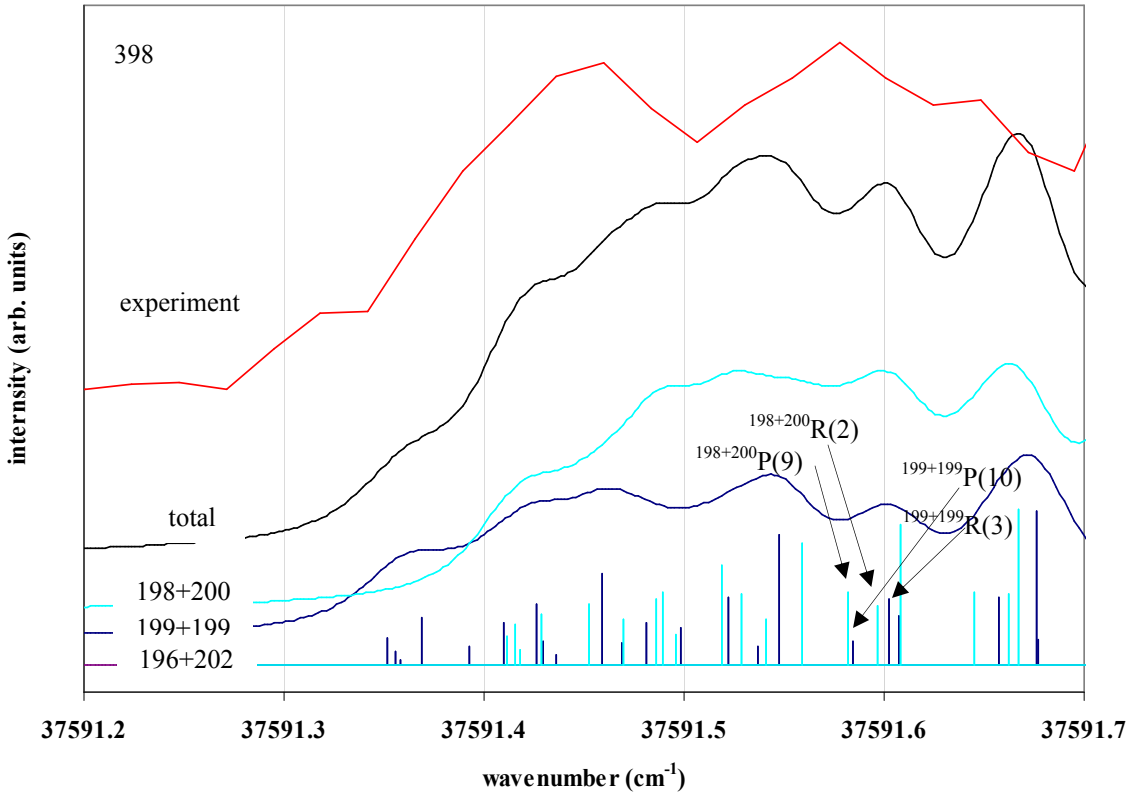

Figure III-8. The locations of the $P(10)$ transition and its adjacent transitions in the experimental and simulated profiles of the A_1+A_2=398 ($^{198}Hg^{200}Hg$, $^{199}Hg^{199}Hg$ and $^{196}Hg^{202}Hg$) isotopic components of Hg_2. $^{198+200}P(9)$ and $^{198+200}R(2)$ are the P(9) and R(2) transitions of the combination $^{198}Hg^{200}Hg$, respectively. $^{199+199}P(10)$ and $^{199+199}R(3)$ are the P(10) and R(3) transitions of the combination $^{199}Hg^{199}Hg$, respectively. Because of the large isotope shift of the $^{196}Hg^{202}Hg$ transitions, no transitions of this isotopomer are visible in the range of the simulation. Simulations obtained for $B_{v'=57}$=0.01788 cm^{-1}, $B_{v''=0}$=0.01295 cm^{-1}, T_r=3.3 K, Δ_{Dopp}=0.02 cm^{-1} and Δ_{las}=0.04 cm^{-1}.

CHAPTER IV

ALEXANDRITE LASER EXPERIMENT

4.1 Alexandrite Laser System and the Experimental Setup

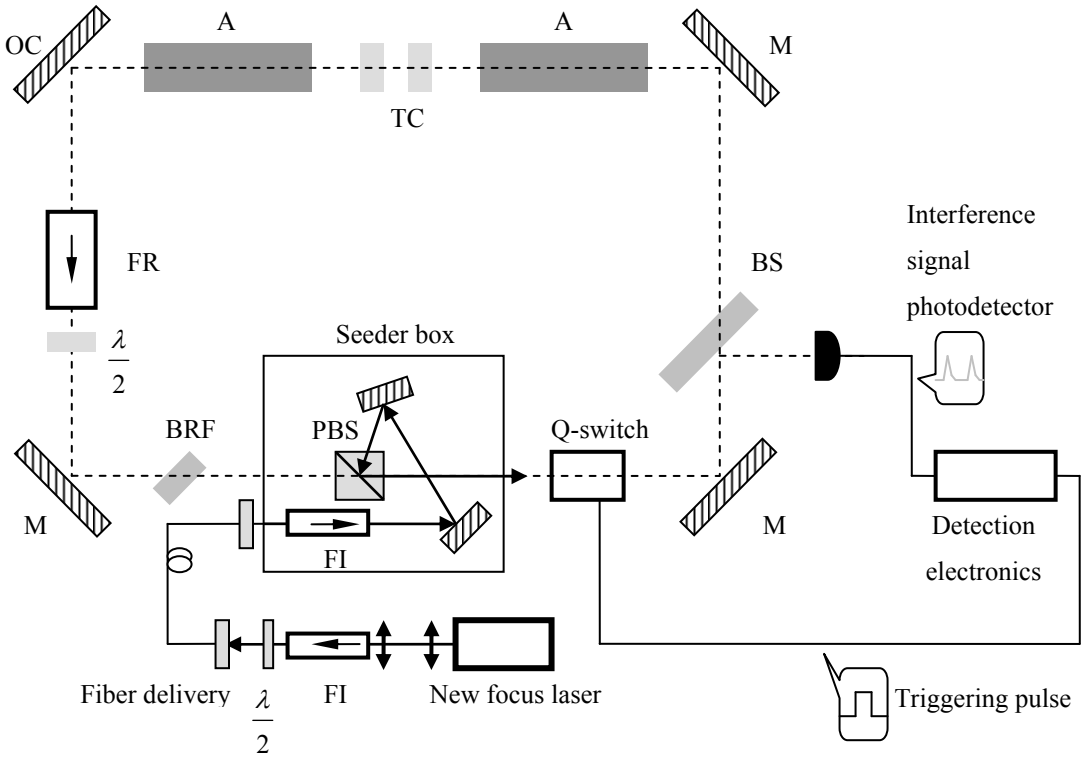

Figure IV-1. Diagram of the alexandrite laser system: A: alexandrite laser rod; BS: beam splitter; BRF: birefringent filter; FI: Faraday isolator; FR: Faraday rotator; M: mirror; OC: output coupler; PBS: polarization beam splitter; TC: thermal lens compensation component which includes a λ/2 plate.

The alexandrite laser system is composed of a commercial PAL 101 systerm (Pulsed Alexandrite) manufactured by Light Age Inc. which serves as a slave resonator and a tunable External Cavity Diode Laser (ECDL) New Focus 6224 which serves as an injection seeder and provides approximately 10 mW at wavelength around 798 nm. The slave resonator has a ring cavity design with two laser rods. The coarse selection of the

longitudinal modes is provided by a birefringent filter (BRF) and the single longitudinal mode operation is achieved by using the ramp and fire technique developed by Henderson et al..[38] A photodetector samples the time dependent interferometric signal leaking out of the cavity which contains peaks separated by one free spectral range of the slave cavity. The peaks occur at the time when the cavity is in resonance with the seeder and the Q-switch will be switched at this time to allow the laser oscillation to build up. See Fig. IV-1 and Fig. IV-2.

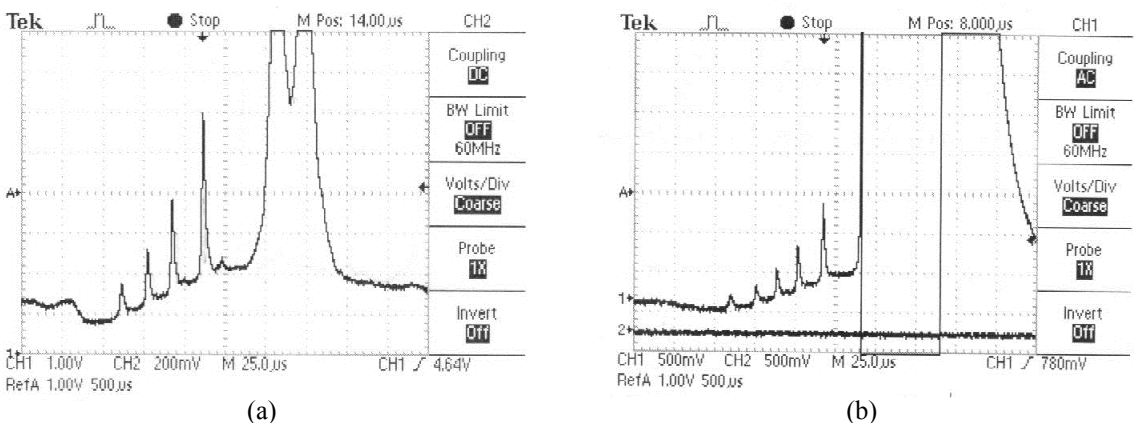

Figure IV-2. Interferometric signal from the alexandrite laser cavity. The vertical axis is the intensity of the interference signal in arbitrary unit and the horizontal axis is the time scale. (a) the Q-switch is off; (b) the Q-switch is switched on and lasing occurs.

The radiation at 266 nm will be produced by third harmonic generation (THG) of the 798-nm output of the pulsed (120-nsec) alexandrite laser operating on a single longitudinal mode with linewidth of 60 MHz. Nonlinear mixing is accomplished in two steps: first, the second harmonic is generated in a lithium triborate (LBO) crystal that is phase matched for type I at 31.9°; second, this doubled requency radiation is sum frequency mixed with the

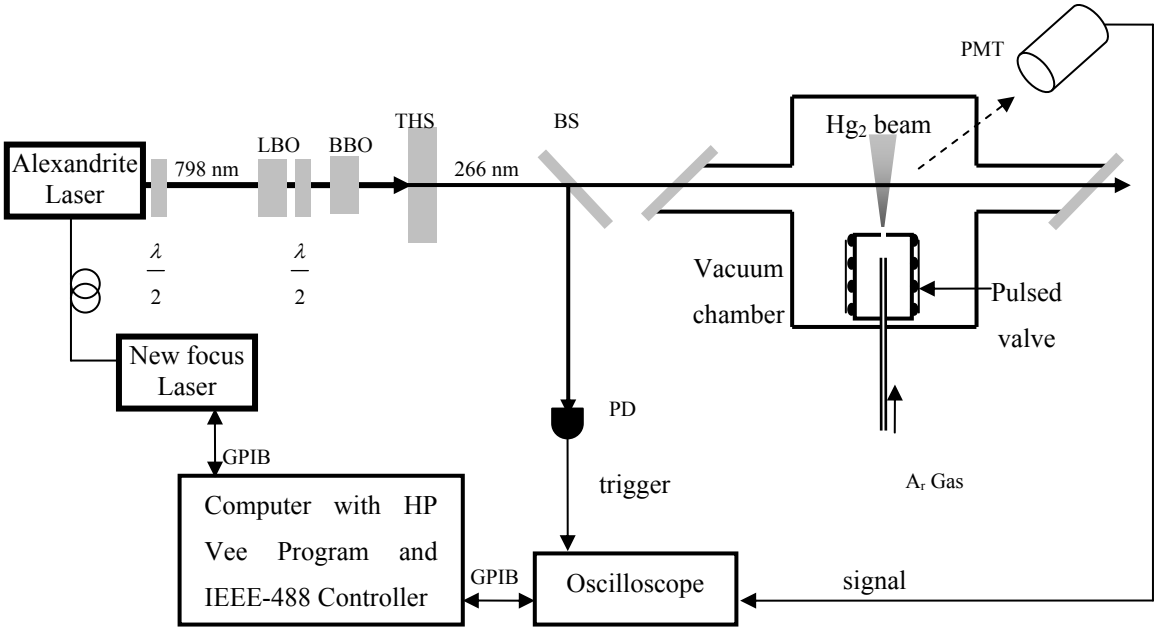

Figure IV-3. Arrangement of the apparatus in the alexandrite laser experiment: THS: second harmonic separator (Pellin-Broca prism set); BS: beam splitter; PD: photodiode; PMT: photomultiplier.

fundamental radiation in a β-barium borate (BBO) crytal that is phase matched for type I at 44.4°. The experimental set up is in Fig. IV-3. The bandwidth of the fundamental wavelength is 60 MHz resulting in a linewidth of 180 MHz for the third harmonic. The experimental setup is similar to that of the dye laser experiment and is shown in Fig. IV-3.

4.2 Data Analysis

In this experiment, only component 402 was able to be measured due to the intensity and the quality of the laser beam. The values of $B_{v'=57}$ and $B_{v''=0}$ were determined using the same simulation and calculation procedure as in dye laser experiment and the results were listed in Table IV-1. The results are different from those obtained in the dye laser experiment but in the range of van Zee's data.[33] The values of $B_{v'=57}$ and $B_{v''=0}$ for other components were

calculated according to Eq. (2.9)-(2.16). Simulations of the 406, 402 and 398 components were performed and compared with the recorded profiles obtained previously in the dye laser experiment. The simulations were shown in Fig. IV-4–Fig. IV-7. These simulations fit the experimental profiles of the dye laser experiment quite well. To improve the reliability and the precision of the results, more data for one component as well as more components are required to get measured. However the wavelength selection by the BRF causes multi-mode oscillation because the transmission bandwidth of the BRF is much wider than the free spectral range of the slave cavity. The laser cavity has been modified to solve this problem.

Table IV-1. B_v values for Hg_2 obtained in the alexandrite laser experiment.

A_1+A_2	$D1_u$	$X0_g^+$
398[b]	0.01570	0.01119
400[b]	0.01562	0.01114
402[a]	0.01554	0.01108
404[b]	0.01546	0.01102
406[b]	0.01539	0.01097

All in [cm^{-1}] unless stated otherwise.

[a] Experimentally determined for $^{402}Hg_2$.

[b] Calculated from the $^{402}Hg_2$ data.

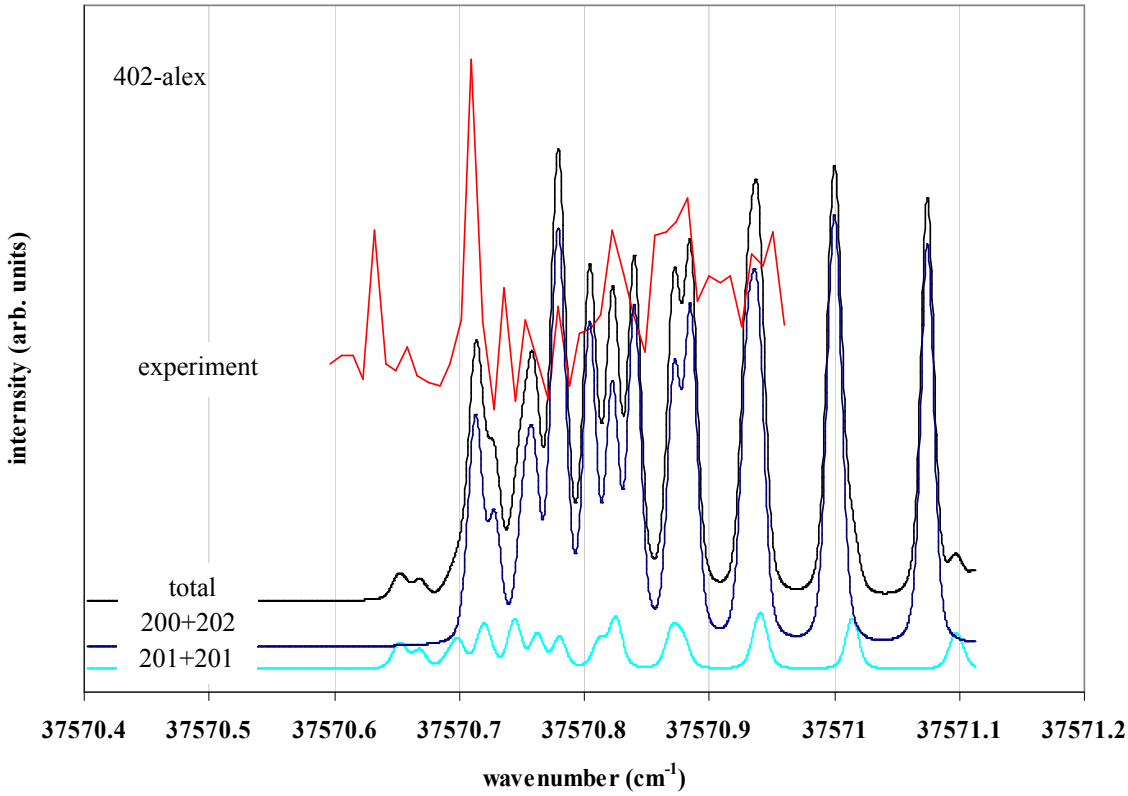

Figure IV-4. The experimental and simulated profiles of the A_1+A_2=402 ($^{198}Hg^{204}Hg$ is out of the simulation range) isotopic components of Hg_2 in the alexandrite laser experiment. Simulation obtained for $B_{v'=57}$=0.01572 cm^{-1}, $B_{v''=0}$=0.01121 cm^{-1}, T_r=0.7 K, Δ_{Dopp}=0.01 cm^{-1} and Δ_{las}=0.004 cm^{-1}.

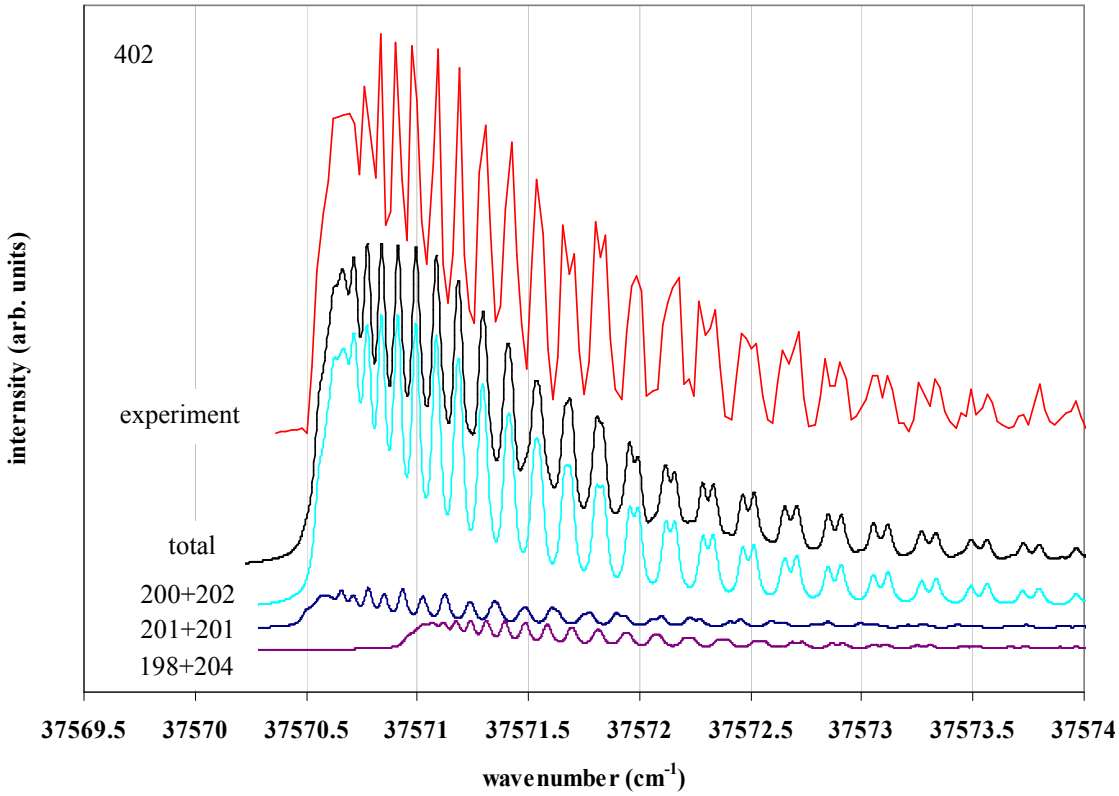

Figure IV-5. The experimental and simulated profiles of the A_1+A_2=402 (^{200}Hg^{202}Hg, ^{201}Hg^{201}Hg and ^{198}Hg^{204}Hg) isotopic components of Hg_2. Simulation obtained for $B_{v'=57}$=0.01554 cm^{-1}, $B_{v''=0}$=0.01108 cm^{-1}, T_r=3.0 K, Δ_{Dopp}=0.015 cm^{-1} and Δ_{las}=0.038 cm^{-1}.

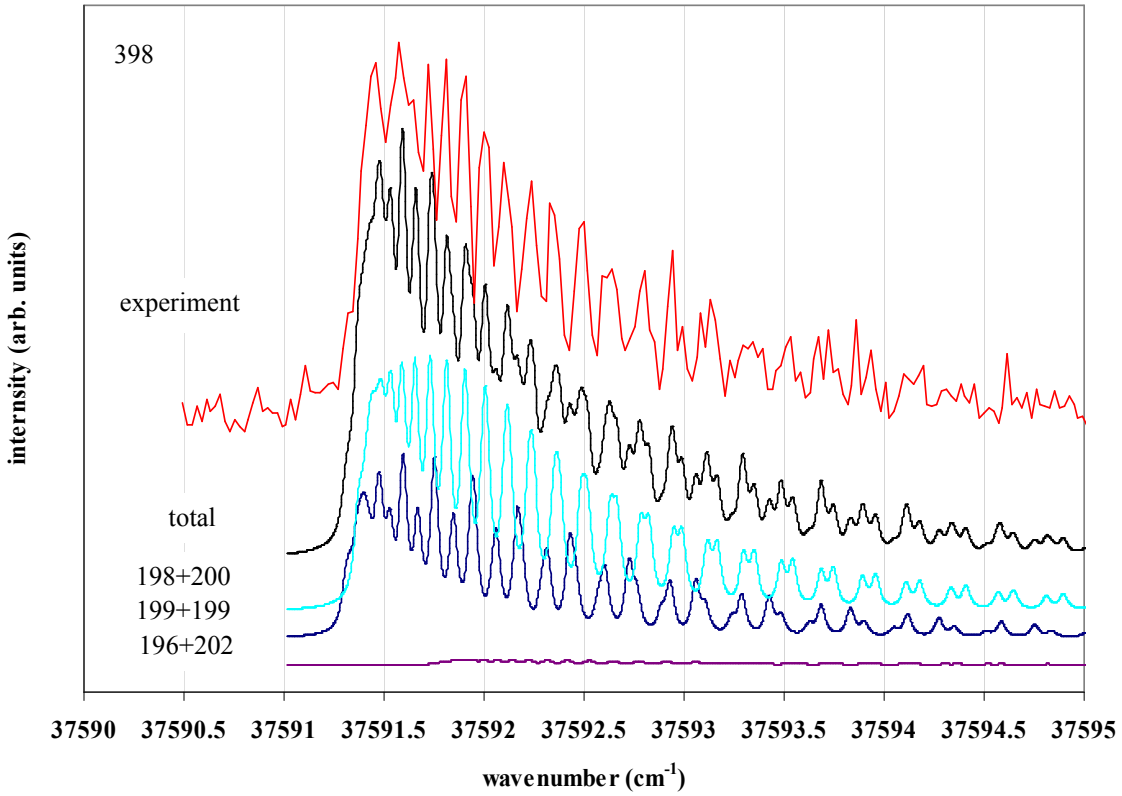

Figure IV-6. The experimental and simulated profiles of the A_1+A_2=398 (^{198}Hg^{200}Hg, ^{199}Hg^{199}Hg and ^{196}Hg^{202}Hg) isotopic components of Hg_2. Simulations obtained for $B_{v'=57}$=0.01570 cm^{-1}, $B_{v''=0}$=0.01119 cm^{-1}, T_r=3.3 K, Δ_{Dopp}=0.02 cm^{-1} and Δ_{las}=0.04 cm^{-1}.

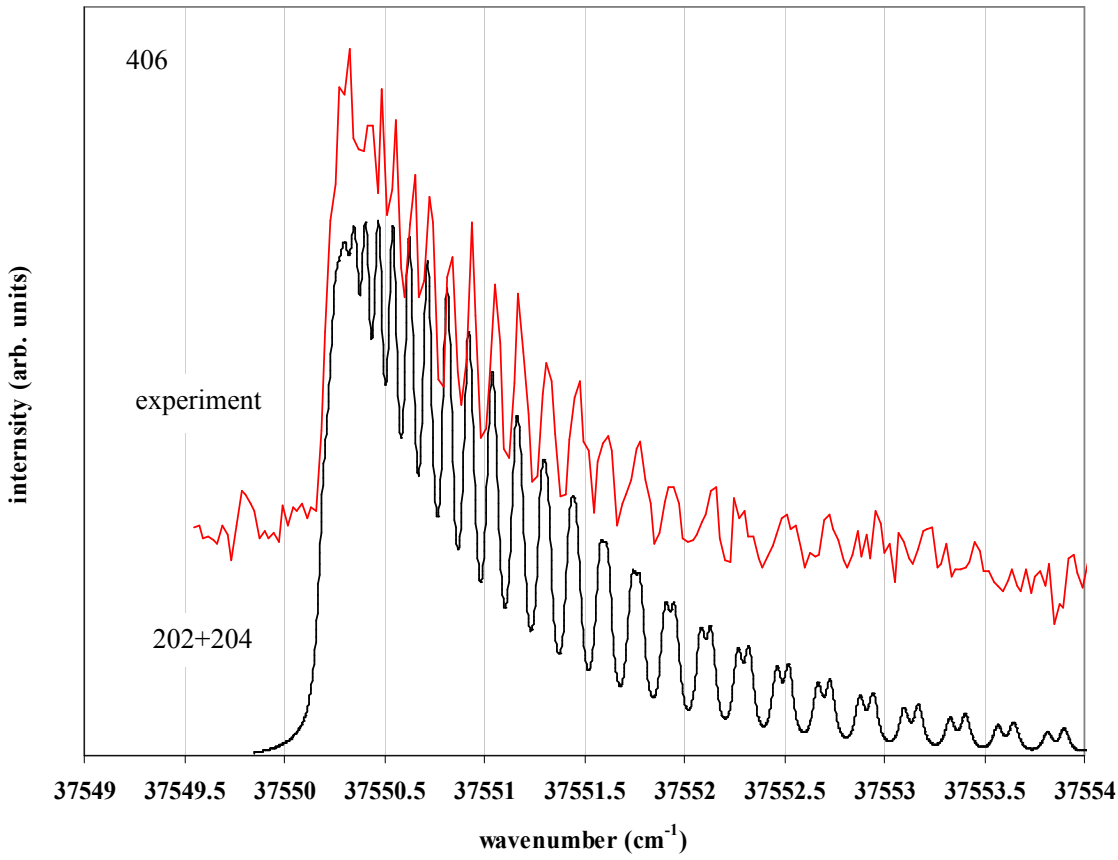

Figure IV-7. The experimental and simulated profiles of the A_1+A_2=406 (^{202}Hg^{204}Hg) heteronuclear isotopomer of Hg_2. Simulation obtained for $B_{v'=57}$=0.01539 cm^{-1}, $B_{v''=0}$=0.01097 cm^{-1}, T_r=3.3 K, Δ_{Dopp}=0.02 cm^{-1} and Δ_{las}=0.05 cm^{-1}.

4.3 Cavity Modification

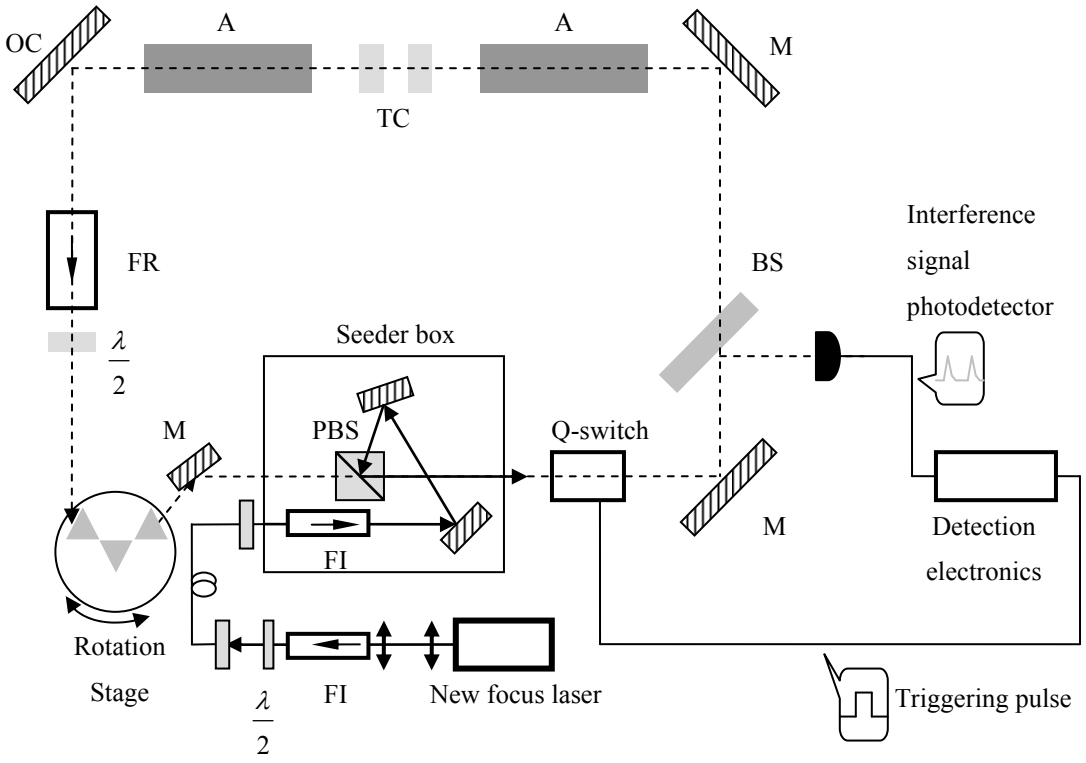

Figure IV-8. Modified cavity for the alexandrite laser: A: alexandrite laser rod; BS: beam splitter; BRF: birefringent filter; FI: Faraday isolator; FR: Faraday rotator; M: mirror; OC: output coupler; PBS: polarization beam splitter; TC: thermal lens compensation component which includes a λ/2 plate.

To reduce the noise in the output of the alexandrite laser and get a continuously tunable single longitudinal mode laser with ultra-narrow line-width, a prism-set composed of three Isosceles Brewster Prisms and a remote controllable rotation stage was inserted into the cavity. See Fig. IV-8. The prism is made of SF10 glass and has an apex angle of 60.6°. Calculations were made carefully for the orientation of the three prisms to obtain the minimum beam deviation at 798 nm. Minimum reflection loss (Brewster angle) on each

incident surface of the prisms for 798 nm was taken into account in the calculation. See Fig. IV-9. Then the prisms were fixed to the rotation stage precisely by using a retro reflection method with a He-Ne laser and a pre-calibrated rotation stage. The prism-set was then mounted on a 3-Dimention adjustable optical mount for the alignment purpose.

Free lasing in the range of 792 nm to 801 nm with coarse tuning was obtained at a much lower threshold than the previous cavity. Single longitudinal seeded lasing was able to be achieved at a certain wavelength. Further effort needed to get continuously fine tuning of the seeded single longitudinal mode lasing.

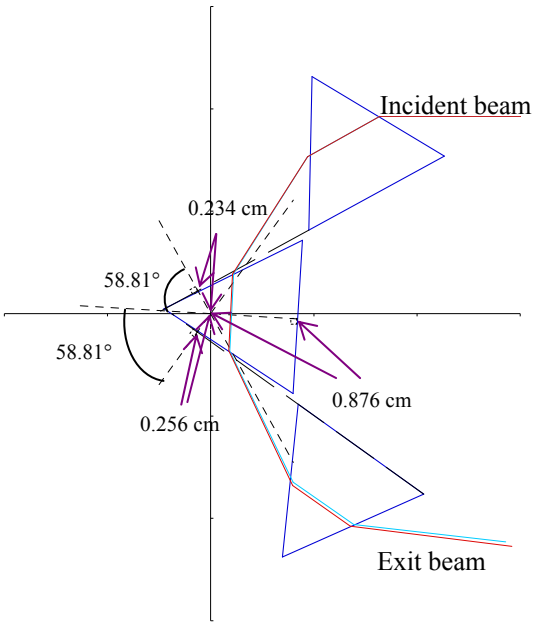

Figure IV-9. Orientation of the three prisms.

CHAPTER V

Ti:SAPPHIRE LASER AND DEFORMABLE MIRROR

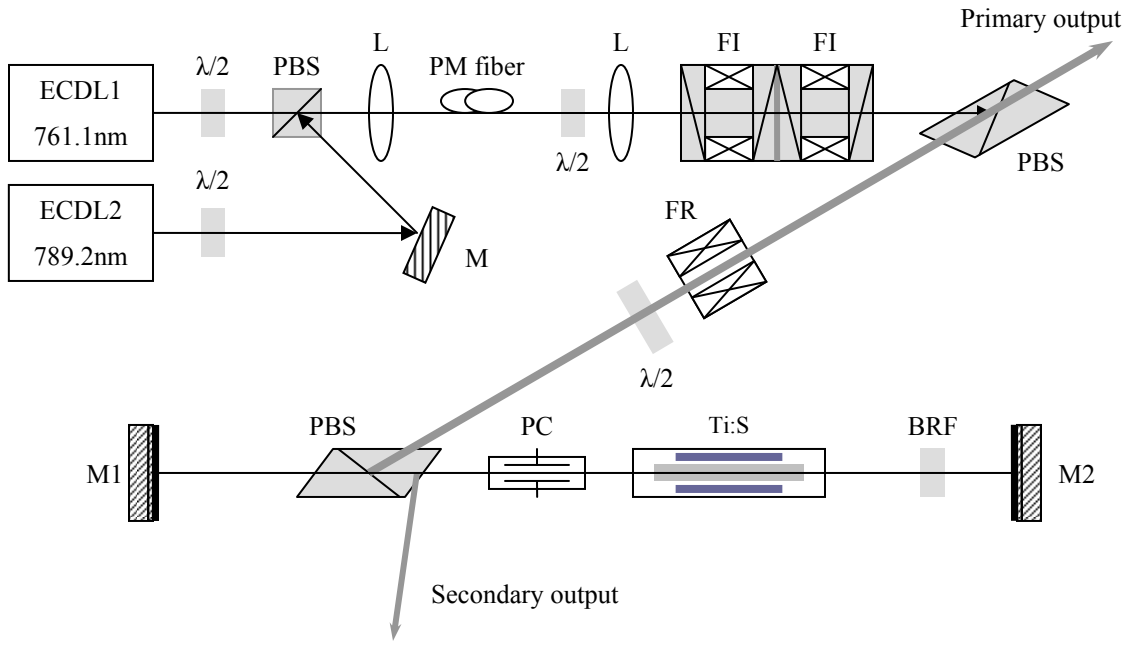

Figure V-1. Ti: Sapphire laser configuration: BS: beam splitter; BRF: birefringent filter; FI: Faraday isolator; FR: Faraday rotator; L: lens; M: mirror; PBS: polarization beam splitter; PC: Pockels cell; PM: polarization-maintaining; Ti:S: Ti:Sapphire laser chamber.

The Ti:Sapphire laser system is composed of a commercial flashlamp-pumped T:Sapphire laser (Elight Laser systems) and two External Cavity Diode Lasers (ECDL) (Sacher Lasertechnik). The configuration is shown schematically in Fig. V-1. The outputs from the two CW diode lasers operating at 789.2 nm and 761.1 nm, respectively, are coupled into a polarization-maintaining single-mode fiber. The output beam from the fiber passes through two Faraday isolators to minimize optical feedback and then is reflected by a polarization beam splitter. After passing through another Faraday rotator and a λ/2 plate, the beam is

finally coupled into the slave laser cavity by a polarizing beam splitter. In the slave laser cavity, the T:Sapphire rod (8-mm diameter, 15cm long) was pumped by four flash lamps. Cavity mirror M1 is flat while M2 has a concave 5-m radius and a thickness of 1mm with twenty set screws pressing against its back to correct the wavefront distortion in the laser rod.[39] The output of the Ti:Sapphire laser is a 4.7-ns pulse with a linewidth of 140 MHz. The Ti: Sapphire laser is chosen for the detection laser in the loophole-free EPR experiment.[16] The third harmonic of 761.1 nm will be applied as the excitation laser (253.7 nm) and the fourth harmonic of 789.2 nm as the ionizing laser (197.3 nm). One LBO crystal that is phase matched for type I at 35.7° and one BBO crystal that is phase matched for type I at 47.5° were used for the third harmonic generating. For the fourth harmonic generating, one LBO crystal that is phase matched for type I at 33° and two BBO crystals that are phase matched for type I at 45° and 67°, respectively, were used. For the harmonic generating, we have the relations

$$I_{2\omega} \propto I_{\omega}{}^{2} \frac{Sin^{2}(\Delta kl/2)}{(\Delta kl/2)^{2}}, \qquad \Delta\vec{k} = \vec{k}_{2\omega} - 2\vec{k}_{\omega}. \tag{5.1}$$

Where $I_{2\omega}$ is the intensity of the second harmonic and I_{ω} is the intensity of the fundamental radiation. We also have

$$I(\vec{r},t) \propto E^{2}(\vec{r},t), \tag{5.2}$$

and

$$E(\vec{r},t) = E_{0}(\vec{r})\cos[\vec{k}\bullet\vec{r} - \omega t + \varphi_{0}] = E_{0}(\vec{r})\cos\varphi(\vec{k}\bullet\vec{r},t). \tag{5.3}$$

Wavefront is the surface of points having the same phase $\varphi(\vec{k}\bullet\vec{r},t)$ at a certain time t and it is perpendicular to the wave vector $\vec{k}$. Fig. V-2 shows the wavefront of a plane wave with and without distortions. According to Eq. (5.1) the wavefront distortion in the

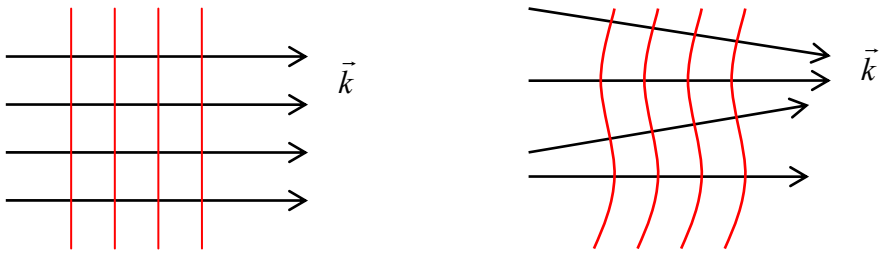

Figure V-2. Wavefront of a plane wave: (a) without distortion; (b) with distortion.

fundamental beam will cause phase dismatching in the harmonic generation precedure. For higher order harmonic generation, this situation gets worse. To improve the beam output of the laser and increase the harmonic generation efficiency, we use a deformable mirror as one of the cavity mirror for the Ti:Sapphire laser. See Fig. V-3 for the working principle of the deformable mirror.

To correct the wavefront distortion with high resolution, we designed a piezoelectric deformable mirror which can provide deformation in microns. The construction of the piezoelectric deformable mirror consists of a very thin mirror (250 microns) coated at 800 nm and 12 × 12 discrete actuators against the mirror surface with a 1 mm center-spacing. The actuators are made of piezoelectric ceramics (EC-65 from EDO Ceramics) which

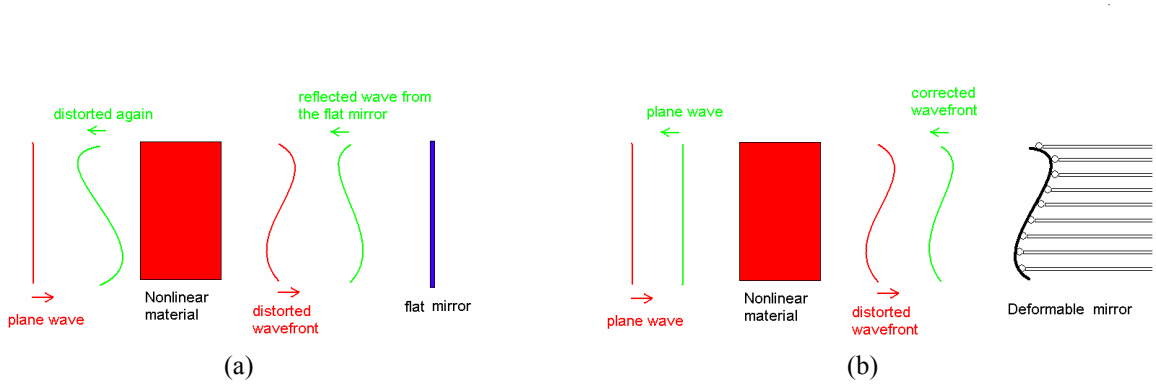

Figure V-3. Working principle of deformable mirror: the wavefront distortion caused by a nonlinear material is independent on the travel direction of the light wave passing through it, (a) reflection from a flat mirror will be distorted more after passing through the nonlinear material the second time; (b) reflection from a correctly deformed deformable mirror will get its wavefront "corrected" after passing through the nonlinear material the second time.

convert the electrical signals into mechanical displacement, see Fig. V-4. Each actuator is connected to the membrane via a small steel ball interface in order to obtain desirable deformation characteristics. The other end of the actuator is bonded to a rigid common base with a compression spring (Century Spring Corp.) and a miniature screw (0000-160 screws from Antrin Miniature Specialities Inc.). The miniature screw will provide about 160 microns displacement per turn. Polyclad laminates with thickness of 300 microns are used for the wiring board; each actuator is wired independently, which provides the ability of independent adjustment.

The actuators are segments cut from the same piece of material in order to obtain as nearly uniform properties as possible. Each actuator is 2.312″ long, 0.015″ thick and 0.030″ wide. With these dimensions, an actuator can have about 6 microns of free displacement at 300 Volts.

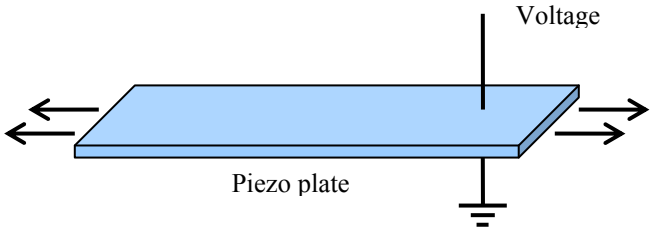

Figure V-4. Working principle of the piezoelectric actuator.

The equation to calculate the free displacement of the actuator is

$$\Delta l_{free} = \frac{l}{t} d_{31} V, \tag{5.4}$$

where l and t are the length and thickness of the actuator, respectively. V is the voltage added along the thickness direction and d_{31} is the piezoelectric constants. For EC-65 type piezoceramics, we have

$$d_{31} = -173 \times 10^{-12}\, m/V \qquad \text{with} \quad V_{\max} = t \times 15\, Volts / 0.001", \tag{5.5}$$

which gives $\Delta l_{free}/V$= 0.02 micron/Volt. To determine the actual displacement Δl_{actual} when working against a mechanical force, a linear interpolation can be made between the zero displacement force F_B and the full displacement zero force.

$$\Delta l_{actual} = \Delta l_{free} (F_B - F_{actual}) / F_B, \tag{5.6}$$

where

$$F_B = d_{31} Y w V. \tag{5.7}$$

Here Y is the Young's modulus and w is the width of the actuator. For EC-65, we have

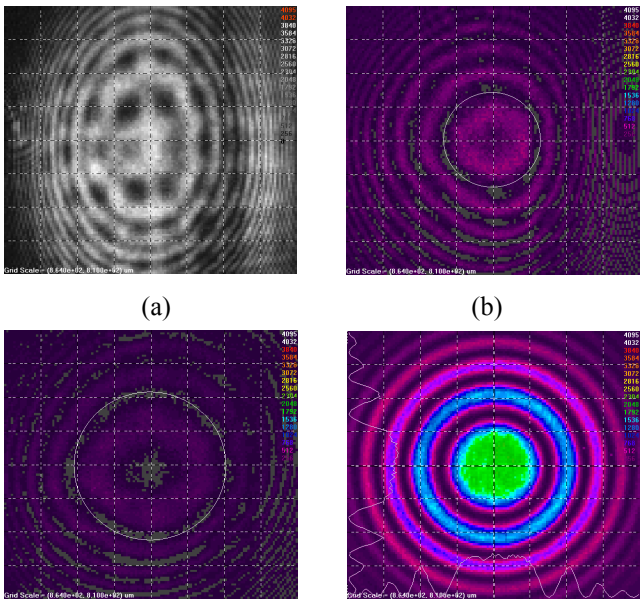

Figure V-5. Surface deformation of the deformable mirror. The interference patterns of the mirror surface at: (a) initial state, using a He-Ne laser; (b) initial state, using the 789 nm ECDL; (c) final state; (d) the interference pattern of a commercial mirror with 5 m radius. The 789 nm ECDL was used in both (c) and (d).

$$Y = 6.6 \times 10^{-10}\, N/m^2, \tag{5.8}$$

which gives F_B/V=0.87 N/Volt. A primary test has been done and the results are shown in Fig. V-5. Because of the Epoxy stress effect,[40] the mirror surface has substructures after its being glued to the actuators. Fig. V-5 (a) gives the interference pattern of the initial mirror surface produced by a Michelson interferometer with a He-Ne laser. Because the mirror is coated at 800 nm, the beam of the He-Ne laser, 632.8 nm, can pass through the mirror surface and make the mirror surface transparent and the actuator grids visible. This provides a coordinate for the actuators. Fig. V-5 (c) gives the interference pattern of the mirror surface after the adjustment of the actuators by applying voltage on corresponding

actuators. Fig. V-5 (d) gives the interference pattern of a commercial mirror with 5 m radius.

Some pictures of the deformable mirror are shown in Fig. V-6.

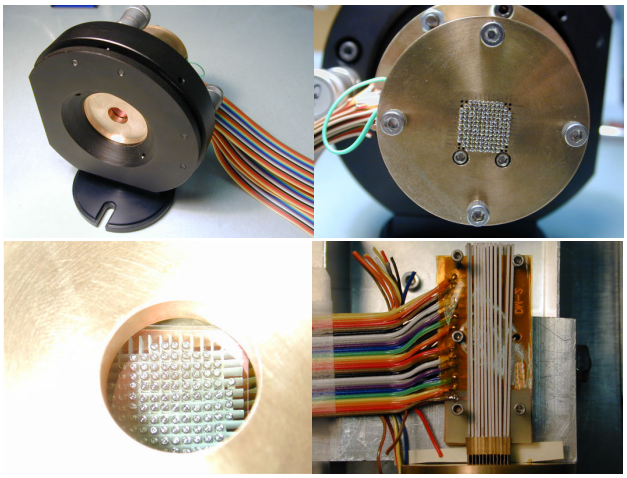

Figure V-6. Pictures of the deformable mirror: front, back, mirror surface glued on a grid of 12×12 steel balls and one of the twelve pieces of piezo stacks.

CHAPTER VI

SUMMARY AND CONCLUSIONS

Rotational profiles in the (57, 0) vibrational band of the $D1_u \leftarrow X0^+_g$ transition in Hg_2 (natural abundance) were recorded and analyzed. The analysis based on Hund's case (c) and all twelve experimentally observable $^{A_1}Hg\,^{A_2}Hg$ components, provided rotational constants and bond lengths for the $D1_u$ and $X0_g^+$ electronic energy states. The values of the $B_{\upsilon'=57}$ and $B_{\upsilon''=0}$ rotational constants of the five A_1+A_2 components were reported. To improve the simulation for each A_1+A_2 components the $D_{\upsilon'=57}$ and $D_{\upsilon''=0}$ centrifugal constants were calculated and implemented. The analysis resulted in the R_e' =2.715±0.010 Å and R_e'' =3.605±0.010 Å bond lengths.

Measurements using a narrow line-width alexandrite laser had been attempted and the values of $B_{\upsilon'=57}$ and $B_{\upsilon''=0}$ were determined. To improve the quality of the laser beam and hence the precision of the rotational constants, modifications have been made to the cavity of the alexandrite laser. This provides a possibility for further investigation.

A piezoelectric deformable mirror was made, having coarse mechanical adjustment and fine electrical adjustment abilities, to improve the output from the Ti:Sapphire laser and increase the harmonic generation efficiency.

REFERENCES

[1] A. Einstein, B. Podolsky, and N. Rosen, "Can quantum-mechanical description of physical reality be considered complete?" Phys. Rev. **47**, 777-780 (1935).

[2] J. S. Bell, "On the Einstein-Podolsky-Rosen paradox." Physics **1**, 195-200 (1964).

[3] J. F. Clauser, M. A. Horne, A. Shimony, and R. A. Holt, "Proposed experiment to test local hidden variable theories," Phys. Rev. Lett. **23**, 880-884 (1969).

[4] J. F. Clauser, and A. Shimony, "Bell's theorem. Experimental tests and implications," Rep. Prog. Phys. **41**, 1881-1927 (1978).

[5] S. J. Freedman, and J. F. Clauser, "Experimental test of local hidden-variable theories," Phys. Rev. Lett. **28**, 938-941 (1972).

[6] J. F. Clauser, "Experimental investigation of a polarization correlation anomaly," Phys. Rev. Lett. **36**, 1223-1226 (1976).

[7] E. S. Fry and R. C. Thompson, "Experimental test of local hidden-variable theories," Phys. Rev. Lett. **37**, 465-468 (1976).

[8] E. S. Fry, "Bell inequalities and two experimental tests with mercury," Quantum Semiclass. Opt. **7**, 229-258 (1995).

[9] A. Aspect, P. Grangier, and G. Roger, "Experimental realization of Einstein-Podolsky-Rosen-Bohm *gedankenexperiment*: a new violation of Bell's inequalities," Phys. Rev. Lett. **49**, 91-94 (1982).

[10] A. Aspect, J. Dalibard, and G. Roger, "Experimental test of Bell's inequalities using time-varying analyzers," Phys. Rev. Lett. **49**, 1804-1807 (1982).

[11] C. O. Alley and Y. H. Shih, "New type of Einstein-Podolsky-Rosen-Bohm experiment using pairs of light quanta produced by optical parametric down conversion," in *Proceedings of the International Symposium Foundations of Quantum Mechanics*, edited by M. Namiki (Physical Society of Japan, Tokyo, 1987), pp. 47-52.

[12] Z. Y. Ou and L. Mandel, "Violation of Bell's inequality and classical probability in a two-photon correlation experiment," Phys. Rev. Lett. **61**, 50-53 (1988).

[13] J. G. Rarity and P. R. Tapster, "Experimental violation of Bell's inequality based on phase and momentum," Phys. Rev. Lett. **64**, 2495-2498 (1990).

[14] J. F. Clauser and M. A. Horne, "Experimental consequences of objective local theories," Phys. Rev. D **10**, 526-535 (1974).

[15] D. Bohm, "The paradox of Einstein, Rosen, and Podolsky," in *Quantum Physics* (Printice Hall, New York, 1951) pp. 611-623.

[16] E. S. Fry, T. W. Walther, and S. Li, "Proposal for a loophole-free test of the Bell inequalities," Phys. Rev. A **52**, 4381-4395 (1995).

[17] C. Tian, Th. Walther, R. Nicolaescu, X.J. Pan, Y. Liao and E.S. Fry, "Synchronous, dual-wavelength, injection-seeded amplification of 5 ns pulses in a flashlamp-pumped Ti:sapphire laser," Opt. Lett. **24** 1496-1498 (1999).

[18] R. K. Tyson, *Principles of Adaptive Optics* (Academic Press, London, UK, 1997) pp. 210.

[19] G. Herzberg, *Molecular Spectra and Molecular Structure* (Van Nostrand, Princeton, NJ, 1950), pp. 148.

[20] P. M. Morse, "Diatomic molecules according to the wave mechanics. II. vibrational levels," Phys. Rev. **34**, 57-64 (1929).

[21] C. L. Pekeris, "The rotation-vibration coupling in diatomic molecules," Phys. Rev. **45**, 98-103 (1934).

[22] J. L. Dunham, "The energy levels of a rotating vibrator," Phys. Rev. **41**, 721-731 (1932).

[23] F. Hund, "Zur Deutung einiger Erscheinungen in den Molekelspektren," Z. Phys. **36**, 637-674 (1926)

[24] J. Koperski, and E. S. Fry, "Molecules in the cold environment of a supersonic free-jet beam: from spectroscopy of neutral–neutral interactions to a test of Bell's inequality," J. Phys. B: Atom. Mol. Opt. Phys. **39** S1125-S1150 (2006).

[25] J. Koperski, "Study of diatomic van der Waals complexes in supersonic beams," Phys. Reports **369** 177-326 (2002).

[26] E. Czuchaj, F. Rebentrost, H. Stoll, and H. Preuss, "Calculation of ground- and excited-state potential energy curves for the Hg_2 molecule in a pseudopotential approach," Chem. Phys. **214** 277-289 (1997).

[27] $c_p/c_v = 5/3$ for a monoatomic gas.

[28] A. Nesmeyanov, *Vapor Pressure of the Elements* (Academic Press, New York, 1963).

[29] Koperski, J.B. Atkinson, and L. Krause, **"**Molecular-beam spectroscopy of the 1(U)(6(3)P(2))-X0(G)(+) and 1(U)(6(3)P(1))-X0(G)(+) transitions in HG-2," Can. J. Phys. **72** 1070-1077 (1994).

[30] C. M. Western, PGOPHER v. 5.1.432, *a Program for Simulating Rotational Structure*, <http://pgopher.chm.bris.ac.uk>, (University of Bristol, UK, 2007).

[31] A. Czajkowski, W. Kedzierski, J. B. Atkinson, and L. Krause, "The rotationally resolved H1u <- AOg+ - electronic spectrum of (202Hg)2," Chem. Phys. Lett. **238** 327-32 (1995).

[32] A. Czajkowski, W. Kedzierski, J. B. Atkinson, and L. Krause, "Rotational analysis of the H1u <- AOg+ - (1,0) bands of (202Hg)2" J. Mol. Spectrosc. **181** 1-10 (1997).

[33] R. D. van Zee, S. C. Blankespoor, and T. S. Zwier, "Direct spectroscopic determination of the ground state Hg_2 bond length and an analysis of the 2540Å band" J. Chem. Phys. **88** 4650-4654 (1988).

[34] The most plausible explanation for the discrepancy between the values of $\omega'_e(F^3 0_u^+)$ and ω''_e in Ref. [53] is a swap of one for another. It is consistent with Morse approximation employed there (see footnote b in Table I of Ref. [33]).

[35] A. Zehnacker, M. C. Duval, C. Jouvet, C. Lardeux-Dedonder, D. Solgadi, B. Soep, and O. Benoist d'Azy, "Experimental study of the cold mercury dimer," J. Chem. Phys. **86** 6565-6566 (1987).

[36] J. Koperski, J.B. Atkinson and L. Krause, "The Ou+(63P1) <- XOg+ spectrum of Hg_2 excited in a supersonic jet," Chem. Phys. Lett. **219** 161-8 (1994).

[37] M. Dolg and H.-J. Flad, "Ground state properties of Hg_2. 1. A pseudopotential configuration interaction study," J. Phys. Chem. **100** 6147-6151 (1996).

[38] S. W. Henderson, E. H. Yuen, and E. S. Fry, "Fast resonance-detection technique for single-frequency operation of injection-seeded Nd:YAG lasers," Opt. Lett. **11**, 715-717 (1986).

[39] X. J. Pan and E. S. Fry, "Use of a deformable mirror for astigmatism correction in a single-frequency Ti:sapphire, flash-lamp pumped laser," in *Conference on Lasers and Electro-Optics*, Optical Society of America, Washington, DC, OSA Technical Digest Series **11,** 143-144 (1997).

[40] R. S. Winsor, A. Sivaramakrishnan, and R. B. Makidon, "Low-cost membrane-type deformable mirror with high-density actuator spacing," in *Adaptive Optical Systems Technology*, P. L. Wizinowich, ed., Proc. SPIE **4007**, 563-572 (2000).

APPENDIX A

HPVEE PROGRAM SAMPLE

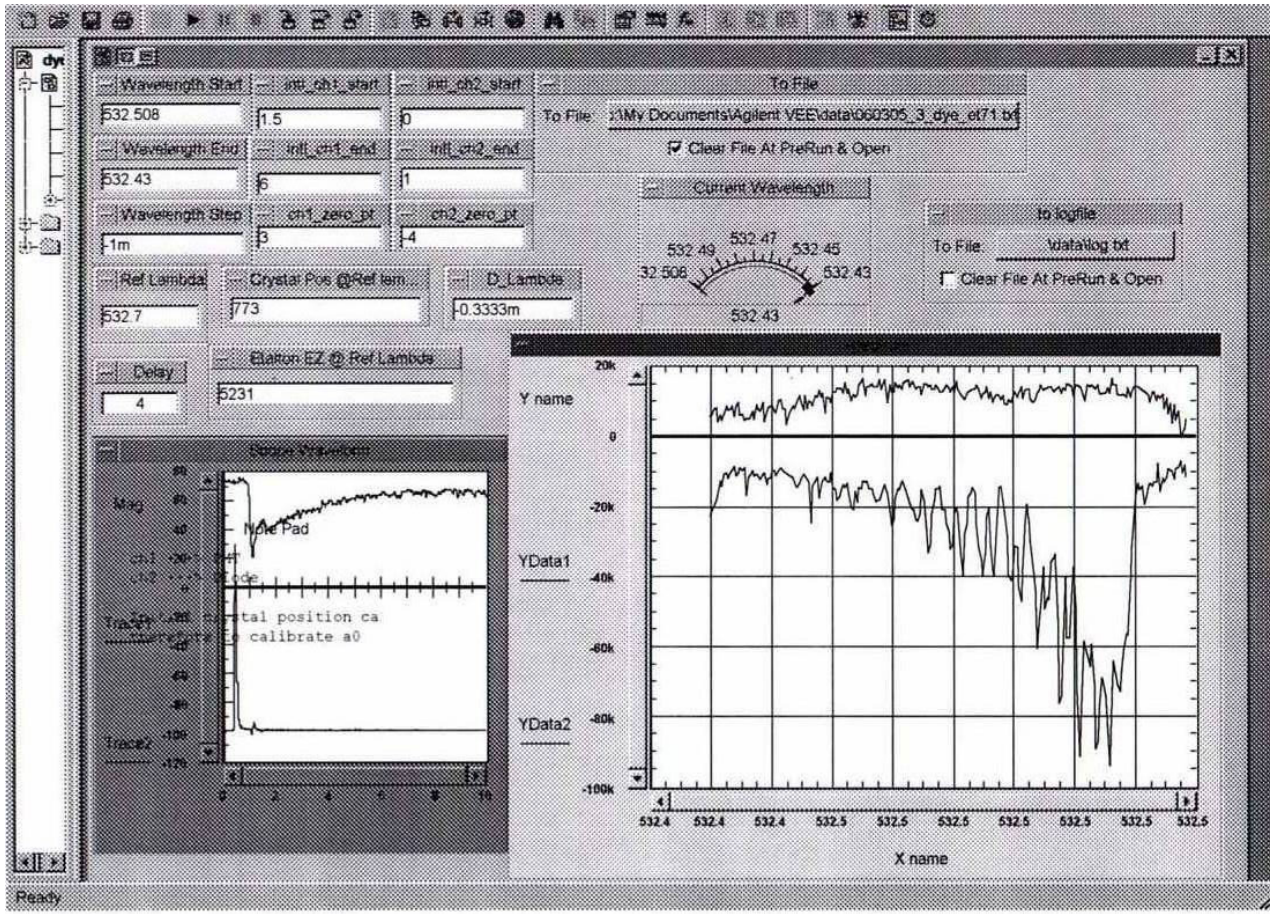

APPENDIX B

ALEX_PAL101 ALIGNMENT

To start the laser

1. Make certain the **INTRACAVITY SHUTTER** on the laser head is in the closed position.
2. Make certain the **Q-SWITCH ON/OFF** and **Q-SWITCH FIRE ENABLE** toggle switches are in the **OFF** position.
3. Turn the external water **ON**
4. Turn **ON** the main system breaker. The base plate heater, tuner heater and harmonic crystal heater are normally turned **ON** all the time.
5. Push the green **COOLING SYSTEM ON** button
6. Wait for the system to warm up; the **WARM UP** light will go out when the water reaches operating temperature and the **ON** button will illuminate.
7. Check to see that the key on the charging power supply is turned to the **ON** position.
8. Press the green **LASER CONTROL READY** button to start the lamp simmer. (It also powers the interlock switch.)
9. Set the **REPEAT/SINGLE/EXT** toggle switch to **REPEAT.** (This switch can be kept in this position all the time.)
10. Set the oscillator and amplifier voltages to correct values (usually the same value for each)

11. Make certain the intracavity shutter switch, located on the front of the laser head is still closed (down).
12. Press the green **FIRE/START** button to flash the lamps or begin a repetition.
13. Set the **FIRE ENABLE** toggles to **ON** for both the pump chambers.
14. Let the flashlamps run for at least 15 seconds before opening the intracavity shutter switch on the laser head to initiate lasing.
15. Once the laser is warmed up, check the laser output power in **LONG PULSE (LP)** operation. If the power is low, adjust the back mirror using a screw driver through the rear ports to maximize power.

To run the laser in seeded mode

1. Once the laser is running in optimum condition in LP mode, the laser can be operated in Q-switched seeded mode.
2. Close the intracavity shutter.
3. Turn **ON** the seed diode laser and check for its correct current setting.
4. Check the toggle switch at the rear of the laser head is set to **SEEDED Q-SWITCH**
5. Check for correct **TUNER** micrometer setting.
6. Check the Q-switch voltage **ADJUST** and **DELAY** controls for proper values.
7. Turn **ON** the flashlamps if they are not already running.
8. Open the intracavity shutter and check the output power. Check the temporal profile of the laser on the oscilloscope (50 ohm setting) for a smooth Gaussian profile.

Hairy/step fluctuations on the profile indicate multimode operation. Adjust the tuner micrometer to bring the laser into single mode operation.

9. If the temporal profile is not a good Gaussian and if unstable, tweaking back mirror may help.
10. If the output power is not stable and random fluctuations occur, check for correct triggering of the Q-switch.

Check for correct seeding and triggering of Q-switch

1. Follow the above (section B) operation procedures to achieve seeded operation, from steps 1-7 except for setting the toggle switch at the rear of the laser head to **NO TRIGGER** mode.
2. Open the intracavity shutter. The laser should not laser. If it does, increase the Q-switch voltage dial setting until no lasing is observed.
3. Connect the Photodiode **(PD MONITOR)** and **Q-SWITCH TRIGGER** signals from the BNC ports at the rear of the laser head to the oscilloscope (both at 1 mega ohm input).
4. Set the time and voltage scale to 20 microsecond and 1 volt per division scales.
5. The PD monitor signal will show the pickup from flashlamp light and the diode seeder beam.
6. While the flashlamps are running (at their set voltages), the length of the laser cavity changes. When the diode laser comes into resonance at periodic cavity lengths, a large spike will be seen on the PD monitor trace. The laser is configured

for the Q-switch to trigger on a selected (optimum) spike within each flashlamp envelope. The timing of the Q-switch trigger is important to extract maximum output energy. A piezo actuator is incorporated in one of the cavity corner mirror to optimize output power, reduce the timing jitter and improve power stability.

7. Trigger the oscilloscope with the **Q-SWITCH SYNC**. signal from the power supply console. A large spike (greater than 1 volt in amplitude) should occur approximately 20 us after the Sync. signal with a jitter of not more than +/- 10 us.
8. The Q-switch trigger signal should appear consistently on the crest of the large spike.
9. If the spike is low in amplitude, try the following:
    - Turn down the Q-switch voltage setting dial, making sure that lasing does not occur.
    - Adjust the tuner micrometer setting
    - Increase the diode current –Do not exceed the maximum value.
    - If the spike amplitude is still low and especially if multiple spikes are seen, then realignment of the seeder beam may be necessary.
10. If the spike is large but the trigger jitter is high or inconsistent, try varying the Q-switch delay to improve the condition.

Changing laser wavelength

The laser wavelength can be changed by changing the tuner micrometer setting and the seeder wavelength. Change the tuner setting while operating in LP and be cautious not to

exceed 4.0 W. Remember the laser gain increases as the wavelength is moved towards 755 nm. It means that a higher output power will be achieved for the same flashlamp voltage setting.

At times, Q-switch operation will yield more power than Long Pulse operation under same operating conditions. Be cautious not to exceed 3.5 W when the laser is Q-switched.

1. Set the wavelength of the diode laser
2. Follow the procedures in Section C to set the oscilloscope to monitor the spike.
3. Since, the diode wavelength has been changed, no spike will be observed on the scope except for the flashlamp fluorescence riding on top of the DC diode output.
4. Adjust the tuner micrometer slowly to coincide with the diode wavelength. Spikes will appear on the scope when the setting is close the required value. Adjust the tuner to achieve maximum amplitude for the spike.

Set-up of He-Ne laser for laser alignment

1. Set up a He-Ne laser beam to go through the center of the rod apertures. The He-Ne must have translation and tilt controls in both the vertical and horizontal axes. A system of 2 mirrors will also do.
2. Align the He-Ne to the thermal lens of each rod by flashing the lamps (one pump chamber at a time) and observing the deviation of the He-Ne at some distance from the laser.
3. Walk the He-Ne beam at different angles through the pump chambers until the effect of the thermal lens deviation is minimized or eliminated. Remember that the

He-Ne must remain in the center of the rod apertures. The He-Ne should be "thermalized" when flashing each pump chamber both separately and simultaneously.

Realignment of the laser (in LP operation)

1. Normally, adjusting the back mirror will be sufficient to bring the laser in alignment. However, in a situation where it does not help and there is a significant drop in the power, then some other minor alignment may be necessary.
2. Make sure laser is operating in **Long Pulse** mode. Remove the laser cover. Adjust the thermal lens and the back mirror. If that does not help, remove the thermal lens from the cavity**. Reduce the flashlamp voltage** below threshold and slowly increase it until the laser output is about 1 watt. Align the back mirror for maximum power. If necessary reduce the flashlamp voltage so that the output power does not exceed 1.5 W. Introduce the thermal lens in the cavity and increase the flashlamp voltage until barely lasing. Adjust the thermal lens (slowly tweaking down flashlamp voltage as system comes into alignment) for maximum power at the nominal flashlamp voltage setting.
3. If the thermal lens is completely out of alignment and no lasing occurs, then align the thermal lens using the Helium Neon laser. (The HeNe should go through the center of the laser rods and the far field spot should have been corrected for thermal lens effects of the laser rods.) Align the thermal lens against the far field spot of the He-Ne beam.

Full alignment of the laser

1. Remove the Thermal lens compensation components from the cavity (Lens located before and between the pump chambers).
2. Set-up the alignment He-Ne laser according to Section E.
3. Flip the pump chambers (the laser rods attenuate the He-Ne beam) and follow the He-Ne around the ring, checking that it passes through all the components centrally. This can be done by using a lens tissue and a white card as shown in Figure B1. The scattered He-Ne light on the white card will outline the aperture of the optical component while the unscattered dot will show the He-Ne path with respect to the aperture.

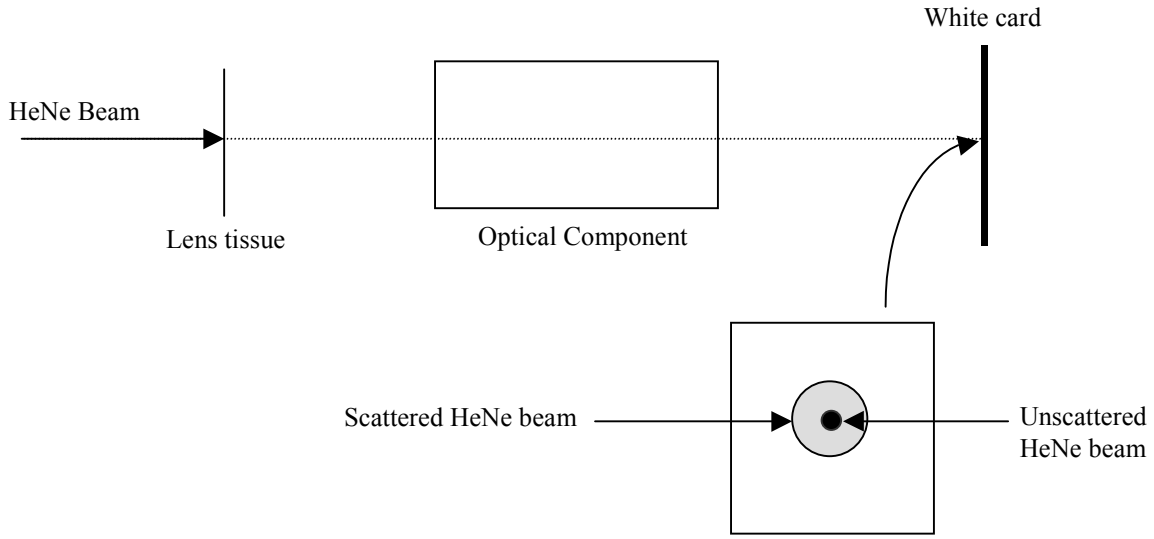

Figure B1. Alignment of the He-Ne laser beam.

4. Being an already aligned system, the He-Ne beam should roughly go through the center of all components. If one or more component is out of alignment, go through the above procedure once again to make sure before either adjusting the relevant corner mirror(s) or the component itself.
5. The decision to either adjust the corner mirror(s) or the component itself should be based on the condition that the laser beam should have the same height around the ring and make 90 degree turns at the corner mirrors.
6. Set up a counter propagating He-Ne beam by establishing a direct retro-reflection with rotator plate located between the pump chambers (by adjusting the rotator gimbal mount).
7. Overlap the 2 counter propagating He-Ne beams: a) inside the injection box and towards the Faraday rotator using the rear mirror and b) at the rear mirror using the piezo mirror.
8. Repeat this step until good overlap is achieved at both locations.
9. Run the laser in long pulse mode and increase the flashlamp voltage gradually until near threshold lasing is achieved. (If no lasing is achieved even at maximum voltage, realign the laser)
10. Align the back mirror for maximum power. If necessary reduce the flashlamp voltage so that the output power does not exceed 1.0 W.
11. If the laser is well aligned, the laser output and the He-Ne reference beam would be collinear in the far field (at least 1 m away from the output port). If they not collinear, check the He-Ne “thermalization” and the laser alignment again.

12. Introduce the thermal lens in the cavity and align it against the He-Ne reference beam. Increase the flashlamp voltage until barely lasing. Adjust the thermal lens (slowly tweaking down flashlamp voltage as system comes into alignment) for maximum power at the nominal flashlamp voltage setting.
13. Note that the thermal lens will magnify any deviation in the collinearity between the laser and He-Ne.

Diode seed laser alignment

1. Remove the aperture/filter assembly from the internal photodiode.
2. With the laser lasing in Long Pulse mode, check that the laser beam from the pick-off plate is hitting the center of the photodiode. Adjust the gimbal mount if necessary.
3. Stop lasing, shut of the lamps.
4. Using the first steering mirror in the injection seeder box, adjust the near field point by aligning the diode beam onto the photodiode.
5. Using the second steering mirror in the injection box, guide the diode beam around the ring and back through the aperture (far field point). An IR viewer will greatly help in locating the beam. The pump chambers may be flipped up during this alignment procedure.
6. Repeat these 2 steps until both the near field and the far field points are optimized. It is often helpful to use a scope monitor and optimize the near field by looking at the DC level from the photodiode.

7. Set the tuner by either the tuning calibration curve or viewing the thru-put of the tuner. Set the tuner to allow maximum diode beam to pass through.
8. With the diode laser aligned to best possible, follow the procedure in Section C to observe the fringes on the scope. Adjust the tuner to maximize the fringes. Walk the diode beam using the steering mirrors in the injection seeder box (horizontal axis first) to improve the fringes. Adjust the pick-of plate if needed. The fringe height should be at least 1 volt above the fluorescence curve.
9. The fringe height can be adjusted using the Q-switch voltage. However, ensure that the voltage is not too low to allow the laser to break through the Q-switch.

VITA

Xinmei Qu was born in Yantai, Shandong, P.R. China, to Shiyu Wang and Weihai Qu. She graduated from the Shandong University in 1996 with a B.S. degree in optics. In July of 1999 she completed a M.S. degree in optical engineer from Shandong University. She married Zheng Lu on 26 July, 1999 and then they came to the United States. They have enjoyed study and research work as graduate students at Texas A&M University. She received her Ph.D. degree in physics from Texas A&M University in August 2008. Her permanent address is 1st Railroad Village, Zhangdian, Zibo, Shandong 255020, P.R.China.